Optoelectronics of Two-Dimensional van der Waals Heterostructures

BY
ROUSAN DEBBARMA
B.Tech., Indian Institute of Technology, Bombay, 2014

THESIS

Submitted as partial fulfillment of the requirements
for the degree of Doctor of Philosophy in Chemical Engineering
in the Graduate College of the
University of Illinois at Chicago, 2020

Chicago, Illinois

Defense committee:
Vikas Berry, Chair and Advisor
Sangil Kim
Alan D. Zdunek
Sanjay K. Behura
Reza Yassar Shahbazian, Mechanical and Industrial Engineering

Contribution of Authors

Chapter 1 is the introduction to my thesis and it includes literature review and an overview of my dissertation. Chapter 2 represents the first project during my Ph.D. which has been published (*ACS Appl. Mater. Interfaces* 2016, 8, 13, 8721-8727) with me as the primary author. Dr. Sanjay Behura, Dr. Phong Nguyen and Dr. T.S. Sreeprasad helped me with some of the experiments shown in figures 1 and 3. My Ph.D. advisor, Dr. Vikas Berry, helped me with the manuscript. Chapter 4 includes the published manuscript (*Nanoscale*, 2018, 10, 20218-20225) for my second Ph.D. project with me as the primary author and researcher. Dr. Sanjay Behura, Yu Wen and Dr. Songwei Che helped me with some of the experiments shown in figures 11 and 12. Dr. Sanjay Behura and my advisor, Dr. Vikas Berry, helped me write the manuscript. Chapters 3 & 5 include unpublished works on WS_2/Graphene and MoS_2/WS_2 heterostructures which will be continued in the laboratory and will be eventually be published with me as a co-author.

Contents

Chapter 1 Introduction 1

1.1 Graphene 1

1.2 Boron Nitride 2

1.3 Transition metal dichalcogenides 2

1.4 van der Waals heterostructures and optoelectronics 3

1.4.1 Light emitting heterostructures 4

1.4.2 2D p-n heterojunction photovoltaics 4

1.5 Preparation of two-dimensional nanomaterials and their heterostructures 5

1.5.1 Mechanical Cleavage 5

1.5.2 Chemical Exfoliation 6

1.5.3 Chemical Vapor Deposition 7

Chapter 2 Electrical Transport and Network Percolation in Graphene and Boron Nitride Mixed-Platelet Structures and the Observation of AC Electroluminescence 9

2.1 Introduction 10

2.2 Experimental 11

2.3 Results and Discussion 14

2.4 Conclusions 24

Chapter 3 Planar and vertical heterostructures of WS_2 with graphene 26

3.1 Introduction 26

3.2 Experimental Section 27

3.3 Results and Discussion 28

3.4 Conclusion 33

Chapter 4 WS_2-Induced Enhanced Optical Absorption and Efficiency in Graphene/Silicon Heterojunction Photovoltaic Cells 35

4.1 Introduction 36

4.2 Results and Discussion 38

4.3 Conclusions 48

4.4 Materials and Methods 49

4.4.1 Synthesis of Graphene on copper foil *via* chemical vapor deposition 49

4.4.2 Transfer of graphene onto *n*-Si substrates 49

4.4.3 Photovoltaic device fabrication 50

4.4.4 Raman spectroscopic characterization 51

4.4.5 Atomic force microscopy 51

4.4.6 Photovoltaic Measurements 51

4.4.7 Absorption Spectra and External Quantum Efficiency Measurements 51
Chapter 5 Temperature and Gate Dependent Photo-response and Valley Coherence in MoS_2-WS_2 heterostructure 52
5.1 Introduction 52
5.2 Results 54
5.2.1 Raman characterization 54
5.2.2 AFM characterization 56
5.2.3 FET conduction mechanism 59
5.2.4 Light response 60
5.2.5 Valley-coherence 61
5.3 Conclusion 62
5.4 Materials and Methods 62
5.4.1 CVD growth 62
5.4.2 FET fabrication and characterization 63
References 64
VITA 75

List of Tables

Table 1: Diode equation parameters, short circuit current density, open circuit voltage, fill factors and the solar cell power conversion efficiencies for the two photovoltaic cells..... 44

List of Figures

Figure 1: Structural Characterizations: High resolution C-1s XPS spectrum of (a) GO with its suspension in brown color, (b) rGO with its suspension in black color and (c) hBN with its suspension in white color, (d) FESEM image of the composite (scale bar is 2 μm) and 2:1 (mL:mL) hBN:rGO nanosheets in DI water in the inset, and AFM topography image of (e) rGO and (f) hBN nanoflakes spin coated on a 300 nm SiO_2/Si substrate. The height profile of a few layer flake shows that the approximate size of a thin flake of both rGO and hBN is about 200 nm. The dashed line represents the nanoflake where the dimension is measured. 13

Figure 2: (a) Raman spectrum of the hBN-rGO composite showing the characteristic rGO and h-BN bands. (b) D and E_{2g}-band position mapping of the composite network with the scale bar showing the Raman shift in cm^{-1}. (c) rGO G band intensity mapping with the scale bar showing the arbitrary intensity units. Coupled with the position mapping in (b), the mixed platelet structure of the composite is confirmed. (d) G-band intensity mapping and Raman spectra of the hBN-rGO composite at two different depths. (e) Tauc plot of the composite showing three optical bandgaps, 4.08 eV and 4.57 eV which correspond to h-BN domains and 2.18 eV which corresponds to rGO domains. Inset shows the Tauc plot of pure rGO and hBN films. 16

Figure 3: (a) Schematic representation of the films along with the electrodes, and a possible platelet arrangement of hBN, and rGO in the composite matrix in the inset. (b) Impedance (Z) versus frequency (ν) plots. The solid lines represent the impedance model of a capacitor (hBN), combination of a capacitor and resistor in parallel (hBN-rGO), and a resistor (rGO). The inset shows the Nyquist plot for the rGO-BN composite which represents a parallel circuit of rGOs (resistors) and hBNs (capacitors) with a poly-dispersed domain arrangements of rGO and hBN. (c) Current-voltage characteristic of the rGO and hBN-rGO composite at ambient conditions. Inset shows the nonlinear I-V characteristics of the hBN-rGO composite. 17

Figure 4: (a) Current-voltage characteristic of hBN-rGO composite at low temperature range (70 – 130 K) and a non-linear fit of the hopping equation provides the mean hopping distance of 1.12

± 0.03 nm, (b) ln(I) versus 1/T plot at different voltages estimates the average thermal activation energy for hBN-rGO composite of 15 ± 0.7 meV, (c) The Poole-Frenkel emission mechanism of hBN-rGO composite at room temperature (300 K) with inset showing the schematic of Poole-Frenkel emission model and (d) Schematic of electron conduction mechanisms between rGO and hBN domains. The grey arrow shows the tunneling of electrons between rGO domains through hBN domains. The green arrow shows the dominant hopping conduction through the trap states of hBN because of the lowering of the barrier by the oxy-based groups. 22

Figure 5: Electroluminescence of the rGO-hBN composite film. (a) Schematic of the EL measurement set up with the composite film connected to a waveform generator and a photodiode a top the film connected to an ammeter. (b) EL response under a sinusoidal wave with a peak-to-peak voltage of 10 V and frequency of 20 MHz. Dependence of EL response on the (c) peak-to-peak voltage and (d) frequency of the sinusoidal voltage applied. 23

Figure 6: a) Schematic representation of the CVD process employed to produce the WS_2/graphene stacked heterostructure. b) Schematic representation of the selective growth of WS_2 on graphene at 900 °C (left) and the onset of WS_2 growth on both graphene and SiO_2 surface at 950 °C (right) 29

Figure 7: Intensity spatial mapping of a-c) graphene G band and d-f) WS_2 PL for the WS_2/graphene heterostructure at three different growth temperatures of 900 °C, 925 °C and 950 °C. The PL mapping shows the onset of WS_2 growth on SiO_2 not covered with graphene at 950 °C. 30

Figure 8: a) Raman and PL spectra of WS_2 on b) graphene and on c) SiO_2 grown at 950 °C at the positions shown by the black and red circles respectively on figure d) which represents the spatial mapping of the WS_2 PL energy showing a red shift in the PL peak energy on graphene. e) Total height of WS_2/graphene vertical heterostructure at the temperature range of 900-950 °C. f) Proposed potential energy profile for the vapor phase precursor adsorbates at 900 °C (top) and 950 °C (bottom). 31

Figure 9: a) Photoluminescence spectra of WS_2 grown at 900° C at parallel and perpendicular polarization orientations. Polar plots for the intensities of the b) WS_2 E_{2g} and c) WS_2 photoluminescence peaks as a function of the polarization angle varied from -90° to 90°. d-f) Polar plots for graphene G peak intensities. The fits follow $\cos^2(\theta-\Phi)$ where θ is the polarization angle and Φ is the phase difference. 33

Figure 10: (a) Schematics of transfer of graphene from Cu foil onto n-Si substrate and (b) CVD synthesis of WS_2 on graphene/n-Si substrate. (c) Schematic of the stacked WS_2-graphene/n-Si heterojunction. 38

Figure 11: (a) Raman spectra of the stacked 2D heterojunction showing the characteristic Raman vibrational bands for WS_2 (E_{2g} and A_{1g}) and for graphene (D, G and 2D) and the photoluminescence peak of WS_2 at 2344 cm^{-1} (2.04 eV). Spatial intensity Raman mapping for WS_2's E_{2g}-band (b) and graphene's G-band (c), respectively. Optical micrographs of WS_2-graphene/n-Si device (d) and WS_2 film on graphene/n-Si surfaces (e). (f) AFM topography image for the WS_2-graphene/n-Si heterostructure. 40

Figure 12: Dark condition current-voltage characteristic curves for (a) graphene/n-Si and (b) WS_2-graphene/n-Si junctions. The black dots show the data points and the red curves represent the fit of the non-linear diode equation. (c) Light condition current density-voltage characteristics under AM 1.5G illumination. (d) Schematic of the energy band structure for the stacked heterostructure. (e) Schematic representation of the photo-generation of the excitons and the separation of electron and hole pairs because of the effective built-in electric field along the direction of the WS_2 layer. 42

Figure 13: Photoluminescence spectra for WS_2 on (a) graphene/n-Si and on (b) SiO_2/Si surfaces. The Lorentzian fits show the neutral exciton (X) and the negatively charged trion (X^-) peaks for both the substrates. The PL spectrum for WS_2 on graphene/n-Si also exhibits the graphene's 2D Raman peak. (c) Absorption spectra for WS_2-graphene and graphene films showing an increased absorption in the WS_2-graphene film in the visible range. (d) External quantum efficiency for the WS_2-graphene/n-Si device. 47

Figure 14: a) Optical micrograph for the CVD grown MoS_2/WS_2 grain. Raman and photoluminescence intensity mapping for b) & c) MoS_2 E_{2g}, d) WS_2 E_{2g}, e) A and f) B peaks. Photoluminescence spectra for g) monolayer and bilayer MoS_2 and h) WS_2 on MoS_2. 55

Figure 15: Raman position mapping of MoS_2 a) A_{1g} and b) E_{2g} peaks and c) their difference. The difference is higher in the folded bilayer MoS_2 and WS_2/MoS_2 regions. Raman spectra for d) WS_2/MoS_2, e) monolayer MoS_2 and f) folded bilayer MoS_2 regions. 56

Figure 16: AFM phase a) & d) and topography b) & d) images for the MoS_2/WS_2 heterostructure. Height profile for c) monolayer and folded bilayer MoS_2 on SiO_2 and f) monolayer WS_2 on MoS_2 57

Figure 17: Phase profile plots for the a) blue and b) red dashed lines shown in figure 16a. c) Roughness histogram showing similar roughness for SiO_2, MoS_2 and WS_2..... 58
Figure 18: Electrical characterization of MoS_2-WS_2 heterostructure. a) The I_{DS}-V_G characteristic for the mixed structure at a bias voltage V_{DS}=5 V and different temperatures (60-200 K). b) The two-dimensional variable range hopping fit of the data obtained in a). c) Current and light response (I_{light}/I_{dark}) as a function of gate voltage at 60 K and d) light response at different temperatures for V_{DS}=5 V. 59
Figure 19: Linear polarization of PL peaks at a) WS_2 and b) MoS_2 domains in the mixed structure. The scattered light is passed through an analyzer that is parallel or perpendicular to the direction of the incident laser. 61

Summary

With the advent and advancement of two-dimensional nanomaterials (2DNM), which can have a wide range of properties, it is important to study routes to build heterostructures to investigate new electronic structures that evolve. The electronic structures can then be manipulated for adding functionalities to 2DNM devices. Van der Waals heterostructures composed of various two-dimensional nanomaterials were assembled and their optoelectronic properties were investigated. Graphene, hexagonal boron nitride (hBN), molybdenum and tungsten disulphide (MoS_2 and WS_2) layers were stacked together and various optoelectronic applications such as light emission, photovoltaic activity, and valley coherence in the mixed layered structures were studied.

In the second chapter a stacked percolating network of semi-metallic reduced graphene oxide and insulating hexagonal boron nitride is prepared *via* chemical and liquid exfoliation techniques. The optical, electrical and structural properties of the mixed hBN-rGO composite are investigated *via* confocal Raman spectroscopy, atomic force microscopy (AFM) and temperature dependent electrical conductivity measurements. It is determined that the transport mechanism is *via* hopping conduction through defect states in the hBN domains. Furthermore, AC electroluminescence was observed in the mixed structure which is attributed to the recombination of electrons and holes in the crystal defects present in the hBN sheets.

In the next two chapters, WS_2 is directly grown on graphene sheets *via* chemical vapor deposition. In the third chapter WS_2 is selectively grown on monolayer graphene grains transferred onto silicon dioxide substrate by controlling the growth temperature. In the fourth chapter, WS_2 is grown on graphene films transferred onto *n*-type silicon substrate forming a photovoltaic cell. The deposition of a few layers of WS_2 atop the graphene layer led to a six-fold improvement in the power conversion efficiency compared to a graphene/silicon cell. This has been attributed to the

Summary

van Hove singularity induced increased light absorption of the WS_2 layer and the reconfiguration of the electronic band structure at the interface.

In the last chapter, a mixed 2D van der Waals structure of the semiconducting transition metal dichalcogenides, MoS_2 and WS_2, are grown *via* CVD and their optical, structural and electrical properties are investigated *via* linearly polarized Raman spectroscopy, AFM and temperature dependent electrical conductivity measurements. A 2D variable range hopping charge transport mechanism was determined *via* temperature dependent conductivity measurements of the field effect transistors with the mixed MoS_2/WS_2 films as channel materials. The FET device also exhibited light effect with the photo-response decreasing with increasing temperature and gate voltage due to the increased occupation of energy states at higher temperatures and gate voltages. Valley coherence was exhibited by the mixed structure which was determined by the polarization of the photoluminescence peak observed when the scattered light is analyzed in a direction parallel and perpendicular to the linearly polarized incident light.

In summary, by stacking various 2DNM, the following were achieved: light emission from the electro-capacitive percolating rGO-hBN structure with hBN as the emission material, improvement in the photoconversion efficiency of graphene/*n*-Si solar cell *via* CVD deposition of WS_2 layers, and valley coherence and strong light response in CVD grown MoS_2-WS_2 field effect transistors.

Chapter 1 Introduction

The separation of a single layer of graphene from graphite back in 2004 has led to an exponential increase in the research of graphene and other two-dimensional nanomaterials (2DNM).[1] The lateral size of 2DNM ranges from a few hundred nanometers to a few microns with thicknesses of the order of only a few angstroms. These 2DNM have revealed exotic physical phenomenon which are sometimes completely different from their 3D counterparts. The research reported in this thesis mainly focusses on graphene, boron nitride, transition metal dichalcogenides and their heterostructures.

1.1 Graphene

Graphene is a single atom thick sheet of carbon atoms arranged in a hexagonal lattice.[1] It has excellent electrical (room temperature charge carrier mobility ~ 10000 $cm^2V^{-1}s^{-1}$), optical (transparency ~98%) and mechanical (Young's modulus ~1 TPa) properties and it also possesses an excellent thermal conductivity (3000-5000 $Wm^{-1}K^{-1}$).[1–4] Its excellent properties combined with exciting physical phenomenon (quantum Hall effect, massless Dirac Fermions, van hove singularity etc.) observed has led to the extensive study of graphene and its derivatives.[5–8] Graphene constrains the motion of electrons in two dimensions and its energy band structure is represented in a two-dimensional Brillouin zone of the momentum space. The Dirac points in the band structure occurs at the K and K′ points of the Brillouin zone where the valance band maxima meet the conduction band minima making graphene a zero-bandgap material.

Although mono- and few-layer graphene is a zero band gap material, large energy gaps have been reported in narrow graphene ribbons.[9,10] In nanoribbons the charge carriers are confined in a quasi-one-dimensional system similar to that of carbon nanotubes. The energy gap can be tuned by controlling the dimensions of the ribbon. Band gap opening on the application of vertical

electric field in bilayer graphene has also been reported in the literature.[11] The presence of multiple oxide groups and defects in graphene oxide nanosheets make them electrically insulating.[12] The introduction of wrinkles in graphene can also lead to band-gap opening.[13]

1.2 Boron Nitride

Hexagonal boron nitride (hBN), also called the "white graphene", is a layered material comprising of layers of boron and nitrogen atoms arranged in a honeycomb lattice. The layers are held together by weak van der Waals forces while the atoms within the layer are covalently bonded. Structurally analogous to graphene, hBN is a wide band gap (5.5-6 ev) insulator.[14] Its atomically smooth surface and the absence of dangling bonds and charge traps makes hBN an ideal dielectric substrate for other 2DNM.[15] Owing to its high band gap, the applications of hBN include deep-ultraviolet-emitter material.[16]

1.3 Transition metal dichalcogenides

The absence of a finite band gap in graphene has led the scientific community to search for other 2DNM. Transition metal dichalcogenide (TMDC), chemical formula MX_2, consists of a transition metal (M) sandwiched between two chalcogen atoms (X).[17] Similar to graphite, the layers of TMDC are held together by weak van der Waals forces and they can be exfoliated mechanically using scotch tape to get few layers of the material.[18] But unlike graphene, most TMDC have a finite band gap and can be used in the design of futuristic ultrathin transistor devices.

Molybdenum and tungsten disulphide (MoS_2 and WS_2) are members of the layered group VI TMDC made up of covalently bonded S-Mo-S/S-W-S sheets with buckled hexagonal lattice held together *via* weak van der Waals forces.[19,20] MoS_2 and WS_2 transition from an indirect bandgap (~1 eV) semiconductor in their bulk forms to a direct bandgap semiconductor with an

energy gap of ~2.0 eV in their monolayer forms. The direct bandgap in monolayer MoS_2 and WS_2 has also enabled the study of the materials for optoelectronic applications.

The excitons in MoS_2 and WS_2 (similar to other group-VI TMDC like WSe_2, $MoSe_2$ etc) emit circularly polarized photons.[21–23] The breaking of inversion symmetry and strong spin-orbit interaction leads to a spin-valley coupling in monolayer MoS_2 and WS_2 which makes it possible to control spin and valley indices of the electrons. The valley index refers to the confinement of electrons or holes in degenerate energy minima of the momentum space. In monolayer WS_2, the edges of the valance and conduction bands occur at the K(K′) points in the hexagonal Brillouin zone. The strong spin-valley coupling in monolayer MoS_2 and WS_2 allows for selective excitation at the K and K′ valleys using left handed and right handed circularly polarized light.

In bilayer WS_2 despite the recovery of inversion symmetry robust valley polarization and valley coherence is observed.[23] This has been attributed to the coupling of spin, valley and layer degree of freedom in the bilayer WS_2 system.

1.4 van der Waals heterostructures and optoelectronics

The ability to combine various 2DNM unlocks a plethora of opportunities in the study and application of atomically thin materials. The 2DNM can be brought together with atomic precision leading to extended range of functionalities and observation of exciting physical phenomena. By stacking layers of 2DNM we can obtain atomically sharp interfaces with large interfacial electric fields opening up opportunities in band structure engineering.[24]

The formation of moiré patterns and a corresponding weak periodic potential on stacking semimetal graphene with the structurally analogous insulating hBN leads to formation of secondary Dirac points.[25] The highest mobility graphene transistors have been achieved by stacking graphene in a hBN sandwich.[26] Field-effect tunneling transistors have been designed by

using hBN as a tunneling barrier between graphene layers.[27] The high band gap and atomically smooth surface of hBN together with a high breakdown field makes it an ideal material to create tunneling junctions. Tunneling based graphene FETs with very high on-off ratios can also obtained by putting a layer of semiconducting TMDC such as WS_2 in between two graphene layers.[28]

The finite layer-dependent band gaps in TMDC allow them to be used for optoelectronic applications. TMDC with different work-functions can be combined to create devices where the electrons and holes can be selectively accumulated in separate layers.[29] Ultrafast charge transfer has been observed between mechanically exfoliated MoS_2 and WS_2 layers.[30] The semiconducting TMDC can also be combined with graphene for photovoltaic applications.

1.4.1 Light emitting heterostructures

Most of the light emitting devices with 2DNM have involved TMDC because of their finite band gap and the intrinsic *p*-type or *n*-type doping of their films. The first report of a 2D-2D light emitting device utilized a *p*-WSe_2/*n*-MoS_2 heterojunction where the electroluminescence was observed because of hot electrons and recombination of electron and hole injected in the individual layers depending on the applied voltage.[31] The electroluminescence intensity was improved by confining the injected charge carriers within the 2D layers. This was shown in a graphene/hBN/monolayer-TMDC/hBN/graphene heterostructure.[32] The graphene layers acts as electron and hole injection layers and the hBN layers help in trapping the injected electrons and holes within the TMDC layer. The light intensity was further improved by repeating the structure and forming multiple quantum wells.

1.4.2 2D *p-n* heterojunction photovoltaics

The ability to form atomically sharp 2D *p-n* heterojunctions can be leveraged for photovoltaic applications. The atomically sharp interfaces ensure that even with a slight mismatch

in energies, the charge transfer will be ultrafast because of the large energy gradient.[30] Gate bias controlled photovoltaic effect has been realized in *n*-MoS_2/*p*-WSe_2 and *n*-MoS_2/*p*-black phosphorus heterostructures.[33,34] In such heterostructures, the photo generated electron-hole pairs are separated at the interface and collected by the electrodes. Graphene can also be combined with various TMDC to obtain photovoltaic devices. By controlling the gate voltage, the graphene layer can act as an electron or hole donor. Graphene heterostructures with WS_2 and MoS_2 have exhibited photovoltaic characteristics.[35,36]

1.5 Preparation of two-dimensional nanomaterials and their heterostructures

One of the biggest challenges in the designing of 2D-heterostructures is the assembling of the various 2DNM in a clean atomically precise manner. Most of the initial studies have involved the mechanical exfoliation of various layers followed by their assembly. The other route that is still in its infancy is the epitaxial growth of 2DNM on top of each other *via* techniques like chemical vapor deposition.

The various methods for synthesizing 2DNM can be broadly classified into the two categories of top-down and bottom-up methods. The most widely studied top-down methods include mechanical cleavage and chemical exfoliation.

1.5.1 Mechanical Cleavage

The most common method of studying a few layers of graphene involves the mechanical cleavage of highly oriented pyrolytic graphite (HOPG) using scotch tapes. The micromechanical cleavage method using scotch tape has been used to exfoliate other 2DNM like hBN, MoS_2, WS_2, $MoSe_2$, WSe_2 etc. from their bulk crystals. This method produces high quality single or few layer nanosheets of various 2DNM. The exfoliated and transferred nanosheets can be observed under optical microscope.[37]

Even though the scotch tape method produces good quality of nanosheets there are a few limitations of this method that prevents it from being used in practical applications. The first major limitation is the low yield of the method which restricts it from being utilized in processes requiring large amounts of the given 2DNM. The second limitation is the inability to control the number of layers of nanosheets which are generally a combination of mono- and few-layers of the exfoliated 2DNM. It is also hard to control the size and the dimensions of the nanosheets using this method. The main requirement for the mechanical exfoliation technique is the availability of the bulk crystals in layered form. Without the layered bulk form, it won't be possible to use the scotch tape method to exfoliate high quality nanosheets. The major limitation of the mechanical cleavage method is the inability to scale up the process for future industrial applications.

1.5.2 Chemical Exfoliation

The problem of the low yield of the mechanical exfoliation method is solved by the higher yield of the chemical exfoliation process. The method usually involves the ion intercalation of layered materials followed by sonication of the intercalated compound to obtain single- or few-layer nanosheets.[38] The modified Hummers method is most commonly used in the production of graphene nanosheets *via* the chemical exfoliation route. It involves the intercalation of bulk graphite flakes in strong acids (H_2SO_4 and HNO_3) followed by treatment with strong oxidizing agents like $KMnO_4$. The intercalated and oxidized graphene sheets are further separated into few-layer nanosheets *via* soncation.[39] Similarly other 2DNM like hBN and TMDC can be exfoliated *via* sonication of bulk crystals dissolved in solvents such N-methyl-pyrrolidone (NMP), dimethylformamide (DMF). The liquid exfoliation of hBN has also been carried out by sonication of bulk hBN powder in deionized water.[38]

Although the overall yield of nanosheets obtained from the chemical exfoliation method is high, the yield of single-layer sheets is still low with relatively small lateral sizes of the sheets. The chemical process also involves the use of toxic organic solvents and strong acids and harmful metal ions used for intercalation.

1.5.3 Chemical Vapor Deposition

The CVD process involves gaseous precursors of the desired nanomaterial being carried to the target substrate or a catalytic surface where single or few layered films are grown.[40] The CVD growth of graphene involves the dissociation of methane gas on catalytic surface (copper, nickel, cobalt etc.) releasing carbon radicals that arrange themselves in a hexagonal lattice to form graphene. The self-limiting nature of graphene growth on the catalytic surface allows for the formation of large area single layer graphene sheets. There have also been a few reports on the direct growth of graphene on dielectric substrates such as silicon dioxide. The CVD method has been employed successfully to produce large area ultrathin layers of various other 2DNM like hBN and TMDC.

The CVD process solves the problem of low yield and control of layer numbers faced by the exfoliation processes. The scalability of the process will enable the use of 2DNM in future industrial applications.

The report is divided into five chapters including the introduction. The second chapter is about the study of optical, structural and electronic properties of chemically exfoliated graphene and boron nitride nanosheets stacked together. The synthesis of the heterostructures, their optical and structural characterization *via* Raman spectroscopy and atomic force microscopy followed by their electrical characterization are discussed in detail. This chapter also looks into the

electroluminescence observed in the stacked composite films *via* the application of sinusoidal AC voltage.

The third and fourth chapters are about the optoelectronics of WS_2/graphene heterostructures obtained *via* the CVD process. In chapter 3, WS_2 layers are selectively grown on graphene grains by controlling the growth temperatures. It is observed that the position photoluminescence peak of WS_2 varies laterally as we move from graphene grains onto SiO_2. These growth method helps in realizing both vertical WS_2/graphene heterostructures and lateral heterostructures of WS_2 with different band gaps. Chapter 4 is about the study of the enhancement in the photovoltaic activity of graphene/*n*-Si structure on depositing WS_2 layers *via* CVD. This section focusses on the synthesis of the heterostructures and the analysis of the atomic scale 2D-interface and its effect on the photovoltaic performance of the structure.

The last chapter reports on the stacked MoS_2/WS_2 structure synthesized *via* atmospheric pressure CVD. The section discusses the optical, structural and electrical properties of the mixed structures obtained *via* Raman and photoluminescence spectroscopy, atomic force microscopy and temperature dependent electrical conductivity measurements. The transistor devices fabricated using the mixed MoS_2/WS_2 structure as the channel material exhibited light response that depended on temperature and gate voltage. Valley coherence between electrons and holes at the K and K′ valleys were also observed using linearly polarized photoluminescence spectroscopy.

Chapter 2 Electrical Transport and Network Percolation in Graphene and Boron Nitride Mixed-Platelet Structures and the Observation of AC Electroluminescence

(Previously published as Debbarma, R.; Behura, S.; Nguyen, P.; Sreeprasad, T. S.; Berry, V. Electrical Transport and Network Percolation in Graphene and Boron Nitride Mixed-Platelet Structures. *ACS Appl. Mater. Interfaces* **2016**, *8* (13), 8721–8727.)

Percolating network of mixed 2D nanomaterials (2DNM) can potentially leverage the unique electronic structures of different 2DNM, their interfacial doping, manipulable conduction pathways and local traps. In this chapter, we report on the percolation mechanism and electro-capacitive transport pathways of mixed-platelet network of hexagonal boron nitride (hBN) and reduced graphene oxide (rGO) – two isostructural and isoelectronic 2DNM and the observation of AC electroluminescence in the mixed structure. The transport mechanism is explained in terms of electron hopping through isolated hBN defect traps between rGO (possibly *via* electron 'funneling'). With optical bandgaps of 4.57 eV and 4.08 eV for the hBN-domains and 2.18 eV for the rGO domains, the network of hBN with rGO exhibits Poole-Frenkel emission based transport with mean hopping gap of 1.12 nm (~hBN trilayer) and an activation barrier of ~15 ± 0.7 meV. Further, hBN (1.7 pF) has 6 folds lower capacitance than 1:1 hBN:rGO, which has two orders of magnitude higher resistance than rGO (1.46 MΩ). The application of sinusoidal AC voltage led to the observation of electroluminescence (EL) in the hBN-rGO composite structure. The EL was observed at high frequencies and the intensity increased with the voltage amplitude. The defects in hBN trap electrons or holes during one half cycle of the sinusoidal voltage which recombine with the injected charge carriers in the second half cycle. These carrier transport and electroluminescence results can be applied to other multi-2DNM networks for development of next-generation functional 2D-devices.

2.1 Introduction

With the ever growing library of two-dimensional (2D) nanomaterials (2DNM) and discovery of their intrinsic properties, there is an increased interest in interfacing (either laterally or vertically) different 2DNM into mixed platelet heterostructures/composites to achieve advanced or superimposed functionalities.[15,24,32,35,41–43] Such composites can intimately modulate and/or evolve new characteristics of the constituent 2DNM and can lead to 2D-devices with designer properties. In this context, graphene synthesized *via* the reduction of chemically exfoliated graphene oxide nanosheets has a multitude of applications either on its own as papers[44] or films[45–47] or as a composite[48–51] with other nanomaterials. The excellent mechanical and electrical properties of graphene have been leveraged to fabricate electrically conductive polymeric[52] and ceramic composites[53]. On the other hand, hexagonal boron nitride (hBN) – the isostructural and isoelectronic insulating counterpart of graphene – has excellent mechanical and thermal transport properties[54]. The hBN-polymer composites using hBN nanosheets exfoliated in solution phase has shown superior thermal properties[55]. In this chapter, we exploit the electrical properties of the conducting graphene and the capacitive characteristics of insulating hBN to form a 2D nanocomposite, which can be represented by a conductor-insulator-conductor (C-I-C) percolation system with a network of tunneling junctions. The insulating hBN nanosheets introduces capacitance into the C-I-C structure and the electronic structure can be well ascribed as a parallel R-C (resistance-capacitance) circuit model. Furthermore, we observed electroluminescence in the composite film upon the application of high frequency AC voltage.

Earlier investigations have looked at the conductive percolation in powdered graphite and hBN systems[56,57]; however the system could not have transport through micron-sized hBN-junctions. In the current study, the nanoscale dimensions of the hBN sheets allow tunneling current

between graphene domains *via* hopping through defects in the hBN sheets. In the literature, electroluminescent 2D heterostructures utilized hBN mainly as a tunneling barrier to trap charges within the emitting 2D layers or as encapsulating layers.[32,58] Here we use the hBN layers as the emission layers. The platelet structure arrangements, optical properties, electrical conduction mechanism and AC electroluminescence of the nanocomposite were evaluated *via* field-emission scanning electron microscopy (FESEM), X-ray photoelectron spectroscopy (XPS), Raman spectroscopy, UV-vis transmittance and impedance spectroscopic analysis and temperature dependent transport measurements. In the earlier studies[59], it has been shown that the conductivity in graphene oxide can also be ascribed to CIC transport with graphene-oxide regime as insulator and graphene regions as conductor: conduction increases and the optical band gap reduces with increased reduction of graphene oxide. The maximum band gap achieved *via* the oxidation and subsequent exfoliation of graphene layers of bulk graphite is in the range of 3.0 - 3.6 eV[60–62]. By mixing nanosheets of conducting graphene and hBN, we can achieve a higher level of control to tune the electronic and optical band structure of the composite material and achieve AC electroluminescence.

2.2 Experimental

Here, we report a facile strategy to synthesize macro-scale composite films of chemically exfoliated reduced graphene oxide (rGO) and hBN as presented in Figure 1a. Modified Hummers[63] method was used to oxidize bulk graphite to graphene oxide (GO) as reported in previous works[39] which involves a two-step process: (1) pre-oxidation of graphite, and (2) oxidation of pre-oxidized graphite. In the pre-oxidation step, 5 g of Mesh 7-graphite flake was mixed with strong oxidizing agents, such as: 33 ml of 68% nitric acid (HNO_3) and 200 ml of 96% sulfuric acid (H_2SO_4). The mixture was immediately put in an ice bath and stirred continuously at 100 rpm for 40 minutes to

pre-oxidize and expand graphite flakes. Subsequently, the pre-oxidized graphite was further oxidized by adding 30 g of potassium permanganate ($KMnO_4$) in the solution. Consequently, $KMnO_4$ reacted with H_2SO_4 to generate active oxidizing species ($Mn_2O_7^-$). The temperature of the mixture was increased to 40 ^oC and it was continuously stirred at 100 rpm for 30 minutes, in which the $Mn_2O_7^-$ ions selectively oxidized unsaturated aliphatic double bonds over aromatic double bonds to form functionalized groups of GO.[64] After an interval of 30 minutes, 100 ml of 10% hydrogen peroxide (H_2O_2) was added to the mixture to quench the oxidation by reducing the excess $Mn_2O_7^-$. Finally the solution was centrifuged at 15,000 rpm for 30 minutes and the supernatant was removed to obtain the GO thin sheets. The GO sheets collected as the residue after the centrifugation were purified by washing thoroughly with DI water and dialyzing (MWCO 2000D) for 24 h and then stored as suspension in DI water. The reduction of GO (rGO) was performed by employing a hydrothermal route[65], where the GO solution was heated at 200 °C for 3 h inside a high-pressure reactor (Parr Instruments). In order to confirm the reduction of GO, the XPS technique was employed to characterize the synthesized GO and rGO. The C-1s XPS spectra for GO and rGO are shown in Figure 1a and b along with their optical images of solution (brown for GO and black for rGO) and corresponding structure schematic. The C-1s spectrum of GO shows different chemical components which can be deconvoluted by the sp^2 carbon component C=C at 284.6 eV peak, sp^3 carbon component C-O (hydroxyl, 1,2-epoxide functionalities) at 286.1 eV peak, and sp^2 carbon component C=O (ketone functionality) at 287.5 eV peak.[66] After the hydrothermal reduction, the C-O peak for rGO significantly decreases (~20%) reflecting that the hydroxyl functional groups in rGO are reduced by [H^+] catalyst to produce H_2O.[65] Further, the overall ratios of sp^2 carbon domain to sp^3 carbon domain are 1 for GO and 2.5 for rGO confirming the partial reduction of GO.[67,68]

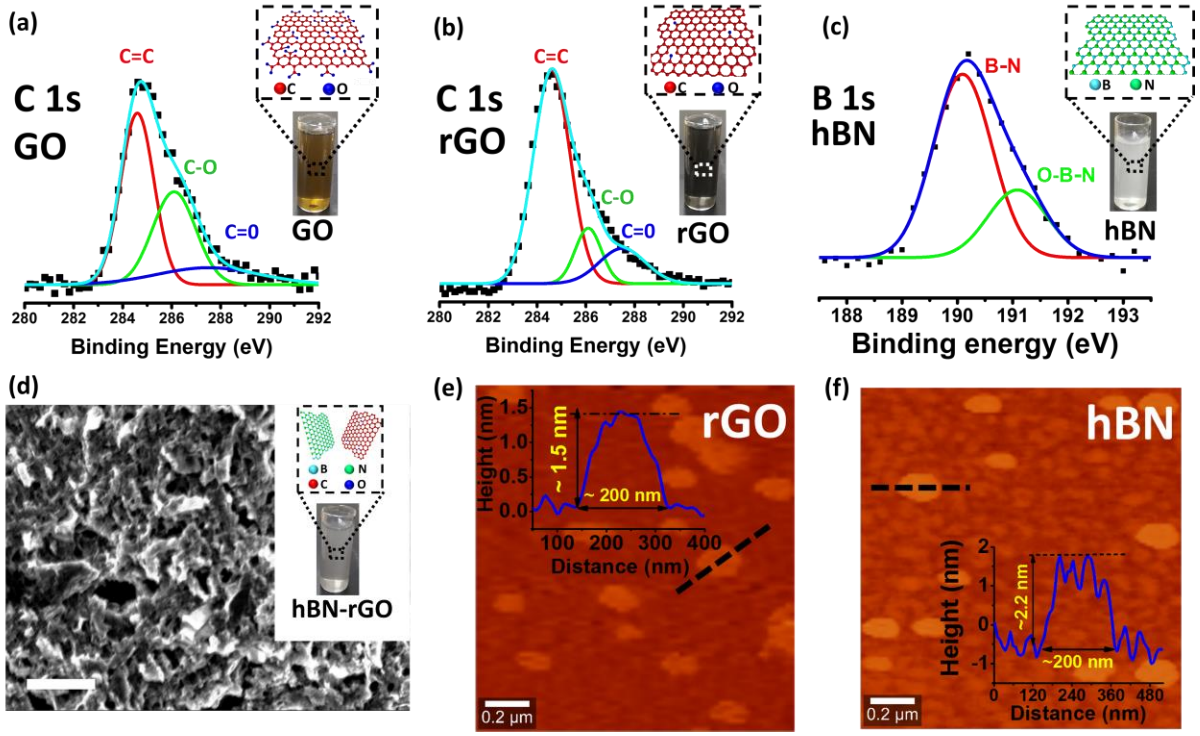

Figure 1: Structural Characterizations: High resolution C-1s XPS spectrum of (a) GO with its suspension in brown color, (b) rGO with its suspension in black color and (c) hBN with its suspension in white color, (d) FESEM image of the composite (scale bar is 2 µm) and 2:1 (mL:mL) hBN:rGO nanosheets in DI water in the inset, and AFM topography image of (e) rGO and (f) hBN nanoflakes spin coated on a 300 nm SiO_2/Si substrate. The height profile of a few layer flake shows that the approximate size of a thin flake of both rGO and hBN is about 200 nm. The dashed line represents the nanoflake where the dimension is measured.

The exfoliation of hBN was carried out through a liquid phase exfoliation procedure reported by Lin et al.[69] Briefly, hBN flakes (200 mg) were dispersed in 100 mL of DI water followed by sonication for 8 h and then the dispersion was centrifuged (10 min, 5000 rpm) and the residue was discarded. Finally, the supernatant was sonicated for 1 h and further used for synthesis of composite with rGO. The B-1s XPS spectra (Figure 1c) shows peaks at 190.5 eV and 191.5 eV, which are attributed to B-N[70] and O-B-N[71] bonding, respectively. The O-B-N bonding peak is seen as the exfoliation of hBN *via* ultrasonication produces boron edges terminated by hydroxyl groups[72]. Further, three different films were prepared from aqueous solutions of rGO and hBN *via* vacuum filtration: (i) rGO film, (ii) hBN film, and (iii) hBN-rGO composite film (1:1 volume ratio). Here, the suspensions were vacuum filtrated through a mixed cellulose ester (MCE)

membrane (Millipore) with 25 nm pores to obtain approximately 1 µm thick films.[44] The volume ratio of the composite has been further confirmed with XPS analysis and the atomic concentration ratio of boron to nitrogen was found to be around 1:1.1 and the ratio of boron and nitrogen to carbon was around 1:2.0. Figure 1d shows the FESEM image of the composite along with 2:1 (mL:mL) hBN:rGO nanosheets in DI water in the inset. As expected, due to the charging of hBN particles, they become brighter under FESEM and the platelet arrangement of hBN, and rGO in the composite matrix is noticed.

The lateral sizes of the nanosheets of both rGO and hBN varied from around 100 nm to ~1 µm as reflected in the AFM topography and the height profile of flakes. Most of the individual sheets of rGO and hBN are expected to be larger than the pore size of the filter paper and therefore, the solvent will escape leaving the sheets on the membrane. Since the process is slow, the sheets will tend to stack reducing the free energy of the system. As pores are occupied by the rGO or hBN nanosheets, the permeation through other pores increases, bringing more rGO or hBN nanosheets, thus balancing the distribution of rGO or hBN to produce a uniform layer (Figure 1d). Eventually, the solvent removal will allow formation of a uniform thin film with continuous coverage. After 12 h of vacuum filtration, the films along with the filter paper were transferred to an insulating substrate (glass slide) for subsequent optoelectronic characterizations.

2.3 Results and Discussion

Raman spectroscopy is a versatile tool for the identification and characterization of the 2DNM. Here we characterize the hBN-rGO composite *via* confocal Raman spectroscopy to determine the spatial arrangement/distribution of 2DNM within the composite network *via* 2D mapping and depth profiling using the confocal Raman system, WITEC Alpha-300-RA, with 532 nm laser and 100X objective lens. The mixed composite film exhibits the characteristic D and G

peaks of rGO positioned at 1350 and 1580 cm^{-1},[73] respectively; while the hBN shows its representative peak at 1366 cm^{-1}, which is ascribed to the E_{2g} phonon mode: analogous to the A_{1g} phonon mode in graphene (Figure 2a).[74] The spatial mapping for the maxima of rGO's D peak and hBN's E_{2g} peak are displayed in Figure 2b, which represents the hBN (yellow and red) and rGO (green and blue) domains. Each pixel represents the position of the maxima between 1320 and 1380 cm^{-1} and thus the pixels with maximum at around 1350 and 1370 cm^{-1} represent rGO and hBN domains, respectively. The spatial distribution of the rGO and hBN domains can be further confirmed by mapping the maximum intensity of rGO's G band as shown in Figure 2c. The hBN regions (yellow domains) in the maxima position mapping in Figure 2b corresponds to the low intensity regions in the rGO's G band intensity mapping in Figure 2c. The vertical arrangement of rGO and hBN domains in the composite has been analyzed by the confocal *z*-depth Raman spectroscopy and depicted in Figure 2d. The *z*-spacing was varied by 50 nm and 10 such frames were acquired and the first and 10th scan which are 500 nm apart are shown. It can be seen that the rGO and the hBN positions have different arrangements in *z* and (*x*, *y*). From the G band intensity mapping of the composite performed at the selected spots (marked by dotted circle), it is seen that the top plane only exhibits the corresponding rGO Raman peak, whereas the bottom plane has both the rGO and hBN peaks. There is a gradual decrease in the G peak intensity of rGO and an increase in the E_{2g} peak intensity of hBN as we go down from the top to bottom plane. After the rGO and hBN aqueous solutions were mixed and sonicated and subsequently filtered, they formed films with random lateral and vertical arrangements of the rGO and hBN domains.

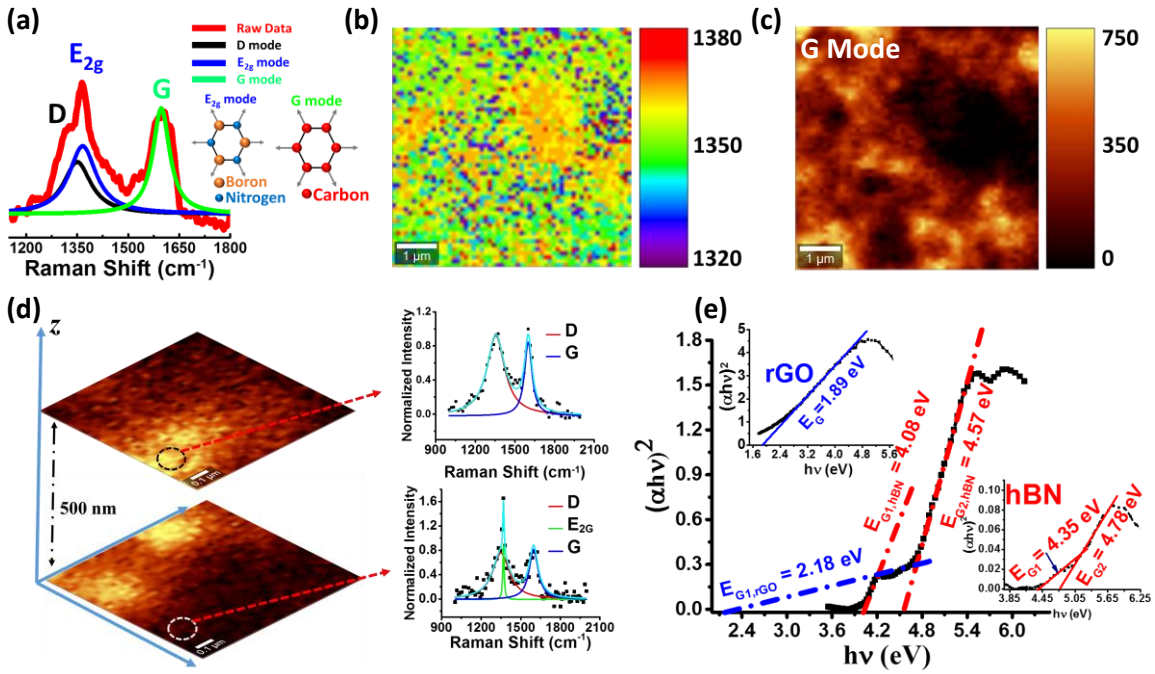

Figure 2: (a) Raman spectrum of the hBN-rGO composite showing the characteristic rGO and h-BN bands. (b) D and E_{2g}-band position mapping of the composite network with the scale bar showing the Raman shift in cm^{-1}. (c) rGO G band intensity mapping with the scale bar showing the arbitrary intensity units. Coupled with the position mapping in (b), the mixed platelet structure of the composite is confirmed. (d) G-band intensity mapping and Raman spectra of the hBN-rGO composite at two different depths. (e) Tauc plot of the composite showing three optical bandgaps, 4.08 eV and 4.57 eV which correspond to h-BN domains and 2.18 eV which corresponds to rGO domains. Inset shows the Tauc plot of pure rGO and hBN films.

The optical bandgaps of rGO, hBN and the composite were determined using Tauc's formulations. For this purpose, the suspensions were spin coated on a quartz slide. To obtain the absorbance, a monochromator (Oriel Cornerstone 130) was employed to irradiate the films on a quartz slide and an empty quartz slide (to obtain base current) with light in the UV region (200-350 nm). The transmitted light was analyzed by means of a photodetector. The Tauc equation[75,76] for direct band gap materials is shown as:

$$(\alpha h\nu)^2 \propto (h\nu - E_g) \quad (1)$$

where α is the absorptivity, h is the Planck's constant, ν is the frequency of the light and E_g is the optical band gap. The optical bandgap is estimated by the x-axis intercept from the linear sections of Tauc plot (shown in Figure 2e). The Tauc plots for the unmixed films, estimated the optical

bandgaps to be 1.89 eV for rGO and two optical bandgaps of 4.35 eV and 4.78 eV for hBN, are shown in the insets of Figure 2e. In the case of the composite, three optical bandgaps were distinguishingly obtained from the Tauc plot. The optical bandgap of 2.18 eV (570 nm) corresponding to the rGO domains, and 4.08 eV (304 nm) and 4.57 eV (270 nm), corresponding to the hBN domains. The optical bandgaps obtained are different from values reported in the literature for rGO[60] (~1.0-2.0 eV) and hBN[77] (~5.5 eV). The decrease in the optical band gap of partially oxidized hBN *via* acoustic irradiation has been reported in a previous study.[77] The change in the optical bandgap of hBN can be attributed to the modification of the electronic structure because of the hydroxyl ending boron edges of the hBN nano flakes, which is similar to the modification of GO bandgap with varying degree of reduction.[60] The modified optical bandgaps of rGO suggests that the hBN-rGO interaction (*via* oxide trap states) modulates their electronic structure. This result further confirms the inclusion of hBN and rGO nanosheets in the mixed platelet composite network.

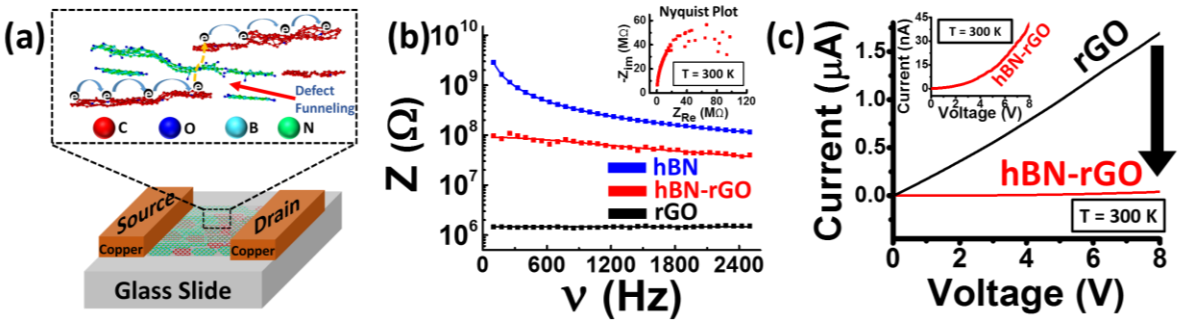

Figure 3: (a) Schematic representation of the films along with the electrodes, and a possible platelet arrangement of hBN, and rGO in the composite matrix in the inset. (b) Impedance (Z) versus frequency (ν) plots. The solid lines represent the impedance model of a capacitor (hBN), combination of a capacitor and resistor in parallel (hBN-rGO), and a resistor (rGO). The inset shows the Nyquist plot for the rGO-BN composite which represents a parallel circuit of rGOs (resistors) and hBNs (capacitors) with a poly-dispersed domain arrangements of rGO and hBN. (c) Current-voltage characteristic of the rGO and hBN-rGO composite at ambient conditions. Inset shows the nonlinear I-V characteristics of the hBN-rGO composite.

The influence of the hBN and rGO hybridization on electrical properties of hBN, rGO, and hBN-rGO composite were characterized for electro-capacitive behavior, DC current-voltage (I-V) behavior, activation barrier and mode of carrier transport. The filtered films were designed into rectangular channels (~50 µm X 150 µm) between copper electrodes on top of the films as shown in Figure 3a. It shows the schematic of the films along with the electrodes, and a possible platelet arrangement of hBN and rGO in the composite matrix. A possible percolating network for electron conduction in the composite device *via* defect assisted inelastic-tunneling (hopping) between rGO sheets through hBN layers is also shown in the inset. The blue arrows represent the electron conduction on the graphenic domains and the yellow arrow shows the process of hopping through the defects on the hBN domains. For spatially ordered rGO-hBN system a C-I-C sandwich structure will be the ideal system to study the conduction mechanism. Recent study on thin graphene-hBN junctions have been done using the metal-insulator-metal sandwich structure.[78] However, in our case we are studying transport through a percolating network of hBN barriers between rGO nanoflakes. The fact that the random arrangement of the nanoflakes of rGO and hBN creates a percolating network at long range shows the efficacy of our system. The C-I-C setup will not represent the intended percolating nature of the composite. The frequency analysis of the AC behavior for the rGO and hBN films and the mixed platelet hBN-rGO composite was performed by impedance measurements through Keysight E4980AL Precision LCR meter. Figure 3b shows the impedance vs. frequency semi-log plot for the three films at a voltage amplitude of 0.5 V. The rGO film represents a truly resistive circuit as the impedance is almost constant (1.46 MΩ) with varying frequency. On the other hand, the impedance of the hBN film decreases monotonically with frequency, mimicking the behavior of a capacitor with the impedance (Z) equal to the reactance, $\chi_C = 1/\omega C$, where ω is the frequency of the sinusoidal voltage source and C is the

capacitance. The calculated capacitance for hBN is 1.73 pF. The Nyquist plot for the composite (inset of Figure 3a) shows a semicircular arc which represents a parallel circuit of a resistor and a capacitor.[79] Thus, the impedance of the composite was modelled *via* a parallel circuit of a resistor and a capacitor, which results the impedance,

$$Z = \frac{R}{\sqrt{1 + \omega^2 R^2 C^2}} \tag{2}$$

where R is the resistance and C is the capacitance. The dispersed points in the Nyquist plot are speculated to be indicators of the varying rGO and hBN domain sizes and their chemistry which is also shown in the Raman mapping of rGO's D band and hBN's E_{2g} band in Figure 2b. The rGO sheets separated by a tunneling barrier of one or few hBN layers can be modelled as resistors and the capacitors and can be represented by thick hBN layers (dielectric medium) separating rGO sheets (conductors). The resistance and the capacitance for the composite were estimated by the fit to the impedance model for the parallel resistor-capacitor circuit. The calculated resistance of the hBN-rGO composite is 99.3 MΩ, which is about two orders of magnitude higher than the resistance of the rGO film (1.46 MΩ). The measured capacitance of the composite is 10.1 pF, which is one order of magnitude higher than that of the hBN film (1.73 pF). The increase in capacitance of the composite can be attributed to the nano-scale hBN domains sandwiched between the rGO domains.

The conduction mechanism in the hBN-rGO composite can be comprehended by analyzing the electronic structure of the rGO and hBN nanosheets, and their influence on each other in the stacked configuration. The rGO has a small band gap of about 1.0 eV[62] compared to the large band gap of 5.97 eV[14] for hBN. The hBN nanosheets produced by sonication assisted hydrolysis contain boron edges with hydroxyl groups due to thermodynamically favorable release of ammonia[72]. Moreover, these hydroxyl groups, the defects in the hBN nanosheets can introduce trap levels

between the valance and conduction band. These trap levels assist in the conduction of charge carriers through the hBN nanosheets; whereas, the oxide groups present in rGO act as barriers to the charge transport (as shown in Figure 1b). Further, the oxy-groups on the hBN and rGO sheets can interact with each other to modulate the electronic structures of both and hence induce doping. The DC *I-V* characteristic behavior was measured *via* Keithley 2612 source meter as shown in Figure 3c. In previous studies[59,80] the *I-V* curves of few layers of rGO (~1 nm thickness) exhibited non-linear behavior. However, the *I-V* linearity for rGO in this case is attributed to the stacking of the rGO layers, which can produce percolating conduction pathways through the conductive graphenic domains. In the stacked composite structure, the conduction of carriers from one rGO sheet to another occurs through a barrier from hBN (one or few layers). This charge carrier transport can take place *via* (a) tunneling through the entire hBN layer(s) and/or (b) hopping through the defect sites within hBN. The latter mechanism is speculated to be more plausible because of a lower energy pathway through hBN defects and hydroxyl groups (significantly reduced barriers). Therefore, in a rGO-hBN-rGO stack within the composite structure most electrons are expected to 'funnel' through spots where the sandwiched hBN has the defect sites[81]. Further, for hBN exfoliated *via* isopropyl alcohol, which induces less defects[38], the conductivity was found to be an order of magnitude lower for the same hBN/rGO ratio. This implies that electron transport is *via* defect assisted tunneling, consistent with a recent study on conduction through hBN junction sandwiched between two metal (Cr/Au) and semimetal (graphite) electrodes.[78] This process would lead the electrons funneling through defect sites of sandwiched hBN platelet to transport from one rGO to the other.

This hopping conduction mechanism explained above is consistent with the observed non-linear *I-V* behavior of the hBN-rGO composite (Figure 4a). Variable low temperature

measurements were carried out to elucidate the hopping conduction mechanism of charge carriers in the hBN-rGO composite (shown in Figure 4a). The hopping charge carriers can: (i) tunnel inelastically (hopping conduction) through the trap barriers at low temperature range or (ii) be thermally excited out of the traps (Poole-Frenkel (P-F) emission) at high temperature range. In the low temperature regime, there exists an increase in conductivity with an increase in temperature (70-130 K). The finite total current as a function of the applied electric field and temperature can be described by the equation,[82,83]

$$I \propto \exp\left(\frac{qaE}{k_B T} - \frac{E_A}{k_B T}\right) \tag{3}$$

where q is electronic charge, a is the mean hopping distance, E is the applied electric field, k_B is the Boltzmann's constant, T is the absolute temperature and E_A is the thermal activation energy for the hopping conduction. The mean hopping distance was determined to a = 1.12±0.03 nm by a non-linear fit of the hopping current equation (3). From the linear fit of *ln(I)* and *1/T* (Figure 4b), the thermal activation energy is estimated to be 15 ± 0.7 meV at various bias voltages. This activation energy of hBN-rGO composite corresponds to the thermal energy at T= 175 K (k_BT = 15.08 meV), signifying that at low temperatures (T<175K), the mode of electron transport must be hopping conduction.

At room temperature (~300 K), Figure 4b showed a thermally activated conduction mechanism which can be modeled by P-F emission[82–84]. The current in P-F emission model is related to the electric field by the relation,

$$I \propto E exp\left(\frac{-q(\Phi_T - \sqrt{qE/\pi\varepsilon})}{k_B T}\right) \tag{4}$$

where $q\Phi_T$ is the trap energy level and ε is the permittivity. From the *ln(I/V)* vs $V^{1/2}$ plot in Figure 4c, it is observed that the hBN-rGO composite exhibits linear dependence, and its conduction

mechanism can be classified as P-F emission. At such high temperature (inset of Figure 4c), the charge carriers of hBN-rGO composite acquire enough thermal energy to overcome the trap energy, which represents the energy difference between the trap states and the bottom of the conduction band.[85] The P-F emission mechanism also involves the lowering of the barrier of charged trap sites as a consequence of Coulombic interactions[84]. This confirms that the solution based exfoliation of hBN creates charged hydroxyl and other oxy-based trap states. Figure 4d reflects the schematic of electron conduction mechanisms between rGO and hBN domains. The grey arrow shows the tunneling of electrons between rGO domains through hBN domains. The green arrow shows the hopping conduction through the trap states of hBN because of the lowering of the barrier by the oxy-based groups.

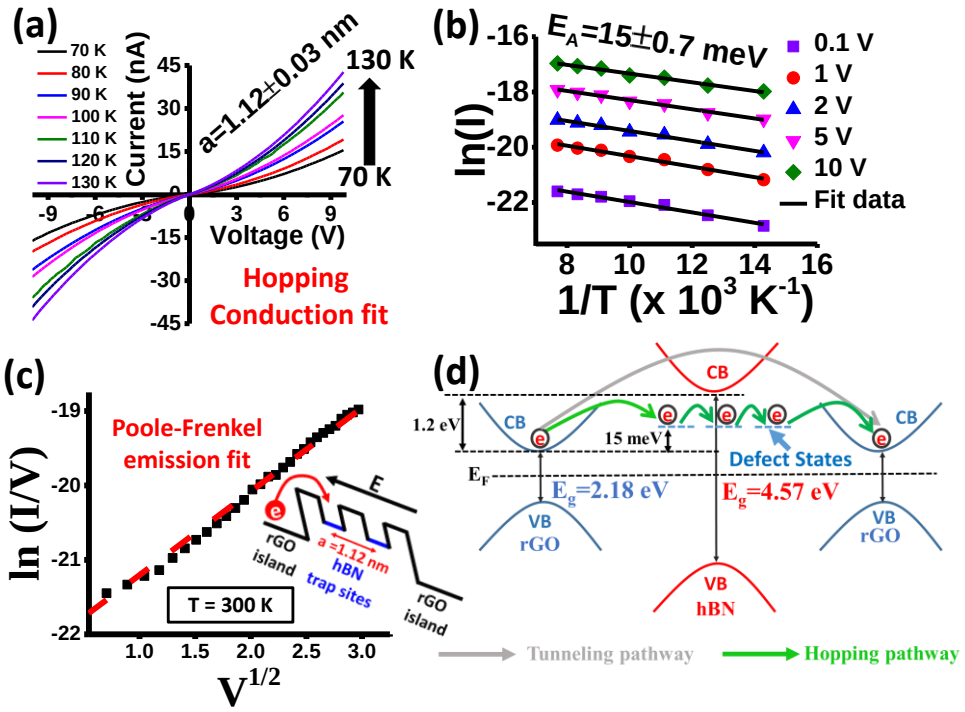

Figure 4: (a) Current-voltage characteristic of hBN-rGO composite at low temperature range (70 – 130 K) and a non-linear fit of the hopping equation provides the mean hopping distance of 1.12 ± 0.03 nm, (b) ln(I) versus 1/T plot at different voltages estimates the average thermal activation energy for hBN-rGO composite of 15 ± 0.7 meV, (c) The Poole-Frenkel emission mechanism of hBN-rGO composite at room temperature (300 K) with inset showing the schematic of Poole-Frenkel emission model and (d) Schematic of electron conduction mechanisms between rGO and hBN domains. The grey arrow shows the tunneling of electrons between rGO domains through

hBN domains. The green arrow shows the dominant hopping conduction through the trap states of hBN because of the lowering of the barrier by the oxy-based groups.

Electroluminescence in the hBN-rGO composite film was observed when sinusoidal AC voltage was applied. The schematic of the experimental set up is shown in Figure 5a where a waveform generator is used to apply sinusoidal voltage and a photodiode connected to an ammeter is used to measure the intensity of the emitted photons. Figure 5b shows the EL response of the composite for a sinusoidal wave with V_{pp}=10 V (peak-peak voltage) and f=20 MHz (frequency). The EL intensity was observed to depend on V_{pp} and f as shown in Figure 5c and 5d respectively. No EL was observed for pure rGO and hBN films under similar voltages and frequencies.

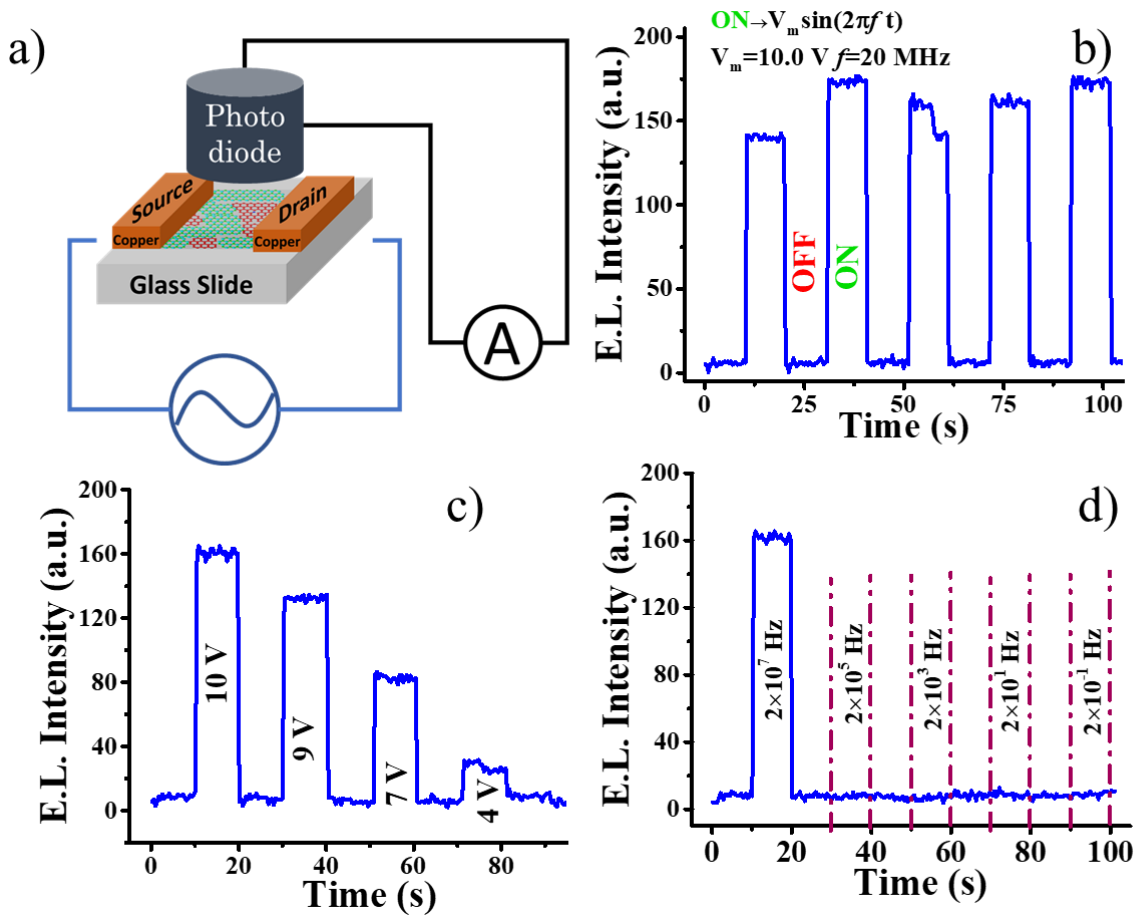

Figure 5: Electroluminescence in the rGO-hBN composite film. (a) Schematics of the EL measurement set up with the composite film connected to a waveform generator and a photodiode

atop the film connected to an ammeter. (b) EL response under a sinusoidal wave with a peak-to-peak voltage of 10 V and frequency of 20 MHz. Dependence of EL response on the (c) peak-to-peak voltage and (d) frequency of the sinusoidal voltage applied.

EL was observed only at very high frequencies of the order of 1E7 Hz. Electrons and holes are injected into the hBN layers from the rGO layers during the negative and positive half cycles respectively and they get trapped in the hBN defects. Similar mechanism has been observed in polyethylene.[86] During the positive half cycles, the injected holes combine with the trapped electrons and vice versa during the negative cycles. This recombination leads to the observed luminescence. The injection of electrons (holes) need to occur before the holes (electrons) can escape the traps *via* thermally excited hopping conduction and move on to the rGO sheets during the second half cycles. In our mixed structures, the hBN flakes are sandwiched between rGO sheets and the charge carriers can move between the rGO sheets by hopping through defects in the hBN sheets as mentioned above in the discussion about the conduction mechanism. At low frequencies, the electrons and holes are excited from the traps before the injection of electrons or holes during the next AC cycle.[87] At very high frequencies, some charge carriers remain trapped and can take part in recombination that leads to electroluminescence. The shallow levels act as traps and the deep levels act as recombination centers. The defect states have wave functions that extends through the momentum space allowing direct transition of electrons and holes and subsequent photon emission.[88]

2.4 Conclusions

In summary, we have investigated the electro-capacitive transport properties of a network of mixed 2D nanomaterials, rGO and hBN, and achieved AC electroluminescence in the composite film. The network includes a conductive rGO separated by defect-mediated hBN funnel sites for electron hopping. Addition of hBN concentration into rGO's complex matrix enhances barrier and

thus resistance; and introduces higher capacitance. The electron transport mechanism developed explains the defects induced junction-barriers and the conduction pathways with transport occurring predominantly *via* hopping conduction at low temperatures and *via* Poole-Frenkel emission at high temperatures. These defect sites further acted as recombination centers for the injected and trapped charge carriers during the half cycles of the sinusoidal voltage leading to AC electroluminescence. Hence creating a randomly stacked structure of hBN and rGO sheets we were able to achieve light emission from the hBN sheets. We envision that this study will allow incorporation of graphene/hBN heterostructures into further applications and will evolve more complex networks of mixed 2D nanomaterials leveraging their respective properties and interfacial doping for advanced/functional 2D-composites.

Chapter 3 Planar and vertical heterostructures of WS_2 with graphene

Quantum mechanical coupling of layered materials opens avenue to leverage the properties of the individual two-dimensional nanomaterials and enable devices with advanced and superimposed functionalities. In this chapter, we utilize graphene grains on SiO_2/Si substrates for the growth of tungsten disulfide (WS_2), a 2D transition metal dichalcogenide *via* chemical vapor deposition. Using graphene as a template and growth temperatures below 950 °C, we have selectively produced WS_2 films just on graphene. At 950°C, growth of WS_2 films were observed both on graphene and on bare SiO_2. Applying the scanning Raman spectroscopic analyses and photoluminescence spectroscopy, we have characterized the optical and optoelectronic properties of the WS_2-graphene hybrid structures. Linear-polarization resolved spectroscopy was performed which revealed the polarization dependent Raman and photoluminescence spectra of WS_2 grown on graphene.

3.1 Introduction

The heterostructures of various two-dimensional nanomaterials (2DNM) can leverage the properties of the individual 2DNM to achieve advanced superimposed functionalities.[24,43,89–91] Transition metal dichalcogenides (TMDC) like MoS_2 and WS_2 are semiconductors with strong room-temperature photoluminescence and band gaps that vary with the number of layers.[18–20] Interfacing a semiconducting (TMDC) 2DNM with a semimetal (graphene) 2DNM can produce interesting electronic and optoelectronic properties.[28,92,93]

The complementary, sizeable and direct band gaps of TMDs, to the gapless graphene has led to multiple studies on TMDC/graphene heterostructures. Similar to graphene, most of the initial studies on MoS_2 were done on samples exfoliated from bulk crystals using scotch tape.[19,94] Reports

on photo-responsive memory device,[95] Schottky barrier transistors,[96] and band offset and negative compressibility[97] of exfoliated MoS_2/graphene heterostructures have demonstrated the unique electrical and optical interactions in TMDC/graphene heterostructures. Although mechanical exfoliation provides us with clean and polymer free samples, in order to utilize the heterostructures in commercial applications the route of chemical vapor deposition (CVD) has to be investigated. There have been studies that reported the growth of MoS_2 *via* CVD on graphene grains as the growth template.[98,99]

A few reports have investigated utilizing WS_2 as a tunneling barrier in a graphene/TMDC/metal or graphene/TMDC/graphene vertical field-effect transistor using mechanically exfoliated WS_2 films.[28,93] In this chapter, we present the first report on the selective growth of WS_2 *via* chemical vapor deposition (CVD) on monolayer graphene grains at temperatures below 950° C. The WS_2/graphene structures have been characterized predominantly employing the versatile Raman spectroscopy technique and atomic force microscopy. We also report the linear polarization resolved Raman and photoluminescence spectra of WS_2 on graphene. The energy degeneracy at the K and K′ points at the edges of the Brillouin zone of TMDC monolayers make them ideal candidates for valleytronic devices[21,22,100]. The broken inversion symmetry in monolayer TMDC and the strong spin-orbit splitting of the valence band maxima allows the control of the valley index of optical phonons using lights of different helicities. Linearly polarized photoluminescence spectra can provide information regarding the coherence or decoherence of photons from the K and K′ edges of the Brillouin zone.[23,101]

3.2 Experimental Section

In order to produce the desired WS_2-Graphene heterostructure, monolayer graphene grains were initially grown *via* chemical vapor deposition technique on copper foil. A 50 µm-thick copper

foil was used as a catalyst substrate and placed inside a 1-inch quartz which was eventually heated to 1100 °C at a pressure of 10 Torr. A constant flow of hydrogen and argon at 300 sccm and 1000 sccm was maintained throughout the experiment and a methane flow of 10 sccm was utilized as a precursor for the graphene growth. Subsequently the graphene on copper foil was transferred onto a SiO_2/Si substrate using PMMA support for graphene and nitric acid as copper etchant. WS_2 was then grown directly on the graphene/SiO_2/Si *via* chemical vapor deposition technique. For the WS_2 growth on graphene/SiO_2/Si, a three zone CVD set up with a one-inch quartz tube was used. Sulfur and WO_3 powders were used as precursors and kept at different crucibles. The sulfur containing crucible was placed in the first zone and the crucible with the WO_3 powder was placed in the third zone of the three zone CVD furnace. The graphene/SiO_2 chip was placed face down over the WO_3 containing crucible. The first zone with sulfur and the empty second zone were heated to a temperature of 200 °C. The third zone was heated to three different growth temperatures of 900 °C, 925 °C and 950 °C. A constant flow of 50 sccm of hydrogen gas and a pressure of 220 mTorr was maintained inside the CVD chamber. After 30 minutes at the growth temperatures, the chamber was allowed to cool down to 700 °C at a slow cooling rate of ~2 °C/min and then fast cooling to room temperature. The hybrid structures were analyzed employing the combined Raman spectroscopy and atomic force microscopy in the WITEC alpha-RA system.

3.3 Results and Discussion

A combined Raman and photoluminescence (PL) spectroscopy are very powerful tools to understand the structural as well as the electronic band structure arrangement in various heterostructures. The spectra were obtained using the WITEC alpha-RA system with a 532 nm laser and a 100X objective. Analyzing the Raman and photoluminescence (PL) spectra we observed that WS_2 selectively grows only on graphene at temperatures of 900 °C and 925 °C.

First we analyze the results for WS_2 grown at a temperature of 900 °C. Raman spectra of WS_2/graphene hybrid structures in Figure 7b exhibits the G band peak corresponding to graphene and the E_{2g}, A_{1g} and the PL peaks corresponding to WS_2. The 2D peak for graphene (~2700 cm^{-1}) cannot be seen in the WS_2/graphene spectra because of the strong PL peak of WS_2 at 2900 cm^{-1} (~ 2.0 eV). We also observe that the Raman spectra on SiO_2 not covered by the graphene grains does not exhibit the signature Raman peaks for either graphene or WS_2. Figure 7c and d show the intensity spatial mapping for the graphene G band and WS_2 PL respectively. The mapping shows that the WS_2 grows selectively on the graphene grains as shown in the Raman spectra in Figure 7b. Similar selectivity of WS_2 for graphene was observed at a growth temperature of 925 °C.

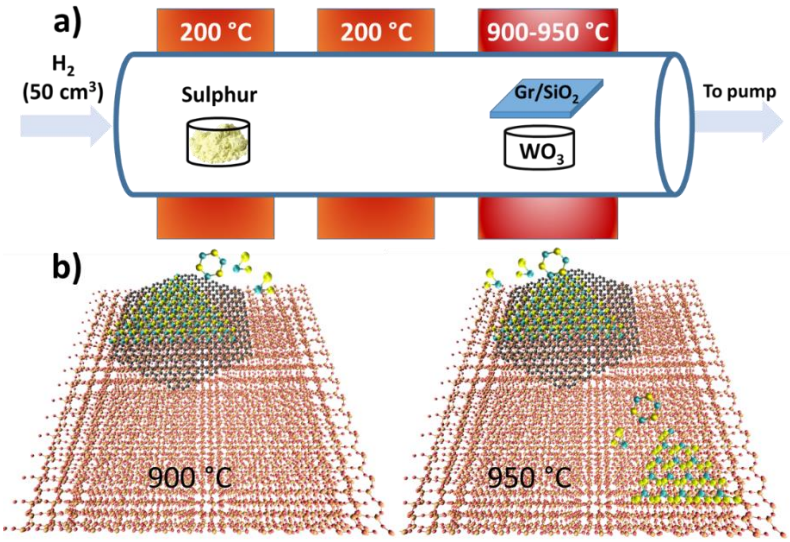

Figure 6: a) Schematic representation of the CVD process employed to produce the WS_2/graphene stacked heterostructure. b) Schematic representation of the selective growth of WS_2 on graphene at 900 °C (left) and the onset of WS_2 growth on both graphene and SiO_2 surface at 950 °C (right)

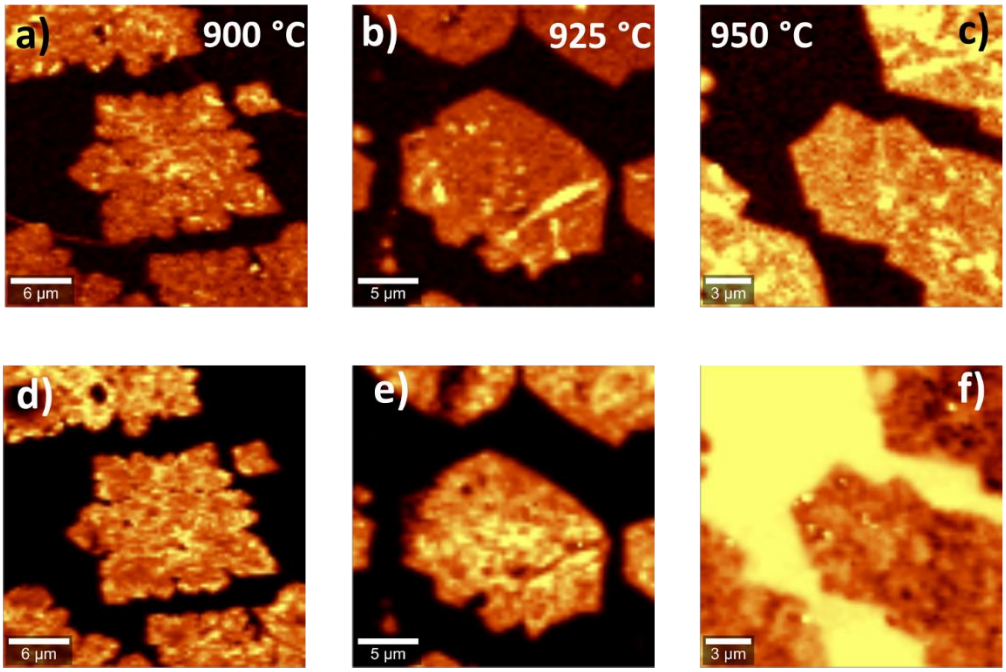

Figure 7: Intensity spatial mapping of a-c) graphene G band and d-f) WS_2 PL for the WS_2/graphene heterostructure at three different growth temperatures of 900 °C, 925 °C and 950 °C. The PL mapping shows the onset of WS_2 growth on SiO_2 not covered with graphene at 950 °C.

Figure 8e shows the height of the WS_2/graphene vertical heterostructure from the SiO_2 substrate at three different temperatures. The total height of around 2 nm indicates the selective growth of monolayer WS_2 on top of graphene grains at a growth temperature of 900 °C. The thickness increased to 5.2 nm at a growth temperature of 925 °C but no WS_2 formed on uncovered SiO_2. On further increasing the growth temperature to 950 °C, WS_2 formed on both graphene and uncovered SiO_2. The total thickness of the WS_2/graphene heterostructure formed at 950 °C was around 5.1 nm. The selectivity below and the saturation in the height above 950 °C can be explained by looking into the energy landscape of the partially covered graphene/SiO_2 substrate. At temperatures lower than 950 °C we can claim that the graphene on SiO_2 provides a lower energy site compared to the uncovered SiO_2 (see Figure 8b). Several density functional theory studies have shown that the hexagonal center in graphene provides a stable adsorption site[102–104]. The precursors at the vapor phase are attracted to the surface by the long range coulombic forces from

the partially charged atoms of SiO_2 and other charged impurities. A neutral graphene in the absence of charged impurities will not contribute to charge screening and so at long ranges the energy for both the graphene covered and uncovered SiO_2 will be similar. But at short ranges, the stable hexagonal center of graphene will further lower the energy for the adsorption of precursors. This lower energy provided by the graphene sites leads to the selectivity at temperatures below 950 °C. A significant lowering in the potential energy minima of the adsorbates can explain the saturation in the total height at 950 °C. In addition to the graphene sites, the adsorbates will have access to the energetically comparable SiO_2 sites to adsorb and nucleate to form WS_2 crystal. From the total height we observed that even at 950 °C graphene still provides the lower energy sites. But the lowering of the potential energy minima on the uncovered SiO_2 sites makes it accessible to the vapor phase adsorbates.

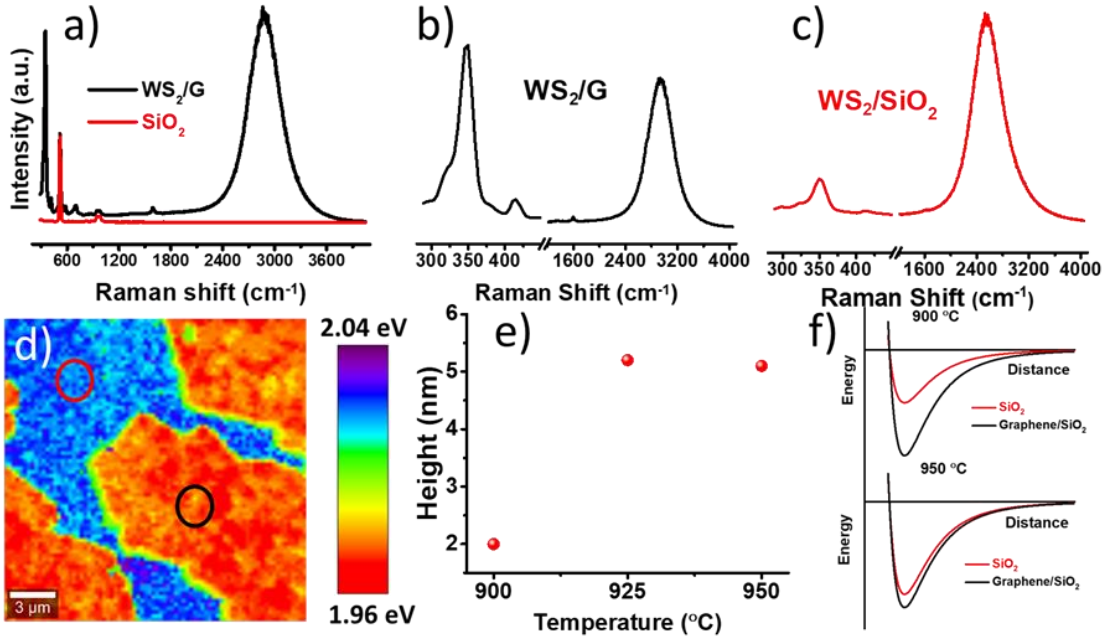

Figure 8: a) Raman and PL spectra of WS_2 on b) graphene and on c) SiO_2 grown at 950 °C at the positions shown by the black and red circles respectively on figure d) which represents the spatial mapping of the WS_2 PL energy showing a red shift in the PL peak energy on graphene. e) Total height of WS_2/graphene vertical heterostructure at the temperature range of 900-950 °C. f)

Proposed potential energy profile for the vapor phase precursor adsorbates at 900 °C (top) and 950 °C (bottom).

The breaking of inversion symmetry in transition metal dichalcogenides (TMDC) allows the use of circularly polarized light to selectively excite electrons from the K and K′ edges of the WS_2 Brillouin zone thereby giving access to the control of valley degrees of freedom.[21,22,100] WS_2 belongs to the same family of TMDC as MoS_2 and similar to MoS_2, the valley degree of freedom in WS_2 can be addressed using circularly polarized light.[23] Since a linearly polarized light can be represented as two circularly polarized light of opposite helicity superposed coherently, it will create electron-hole pairs on both the K and K′ points and the coherence of the photons from the two points of the Brillouin zone can be investigated. Linearly polarized light was shined onto the sample surface by guiding the excitation laser light through a half-wave plate (λ/2). At a fixed incident polarization, the backscattered Raman signal was guided through another half-wave plate and the polarization data was obtained by changing the angles on this collector wave plate form -90° to 90°. Figure 9a shows the photoluminescence spectra for WS_2 grown at 900 °C (monolayer) at parallel and perpendicular orientations with respect to the excitation polarization. The degree of linear polarization, $P = \frac{I(90)-I(0)}{I(90)+I(0)}$, was calculated to be 3.5%. The low degree of polarization can be attributed to decoherence of the photons because of scatterings. The excited electrons quickly relax to the band edge through successions of elastic and inelastic scatterings and then combine with the holes to emit photons. The phase information is generally lost during the random scatterings and so there is a loss of coherence. The measurements were done using a 532 nm (2.33 eV) laser (off-resonance) at room temperatures and that can cause increased scatterings because of phonons and lead to decoherence and low degree of linear polarization. Figure 9b and c show the polar plots for the normalized intensities of the E_{2g} Raman peak and the photoluminescence peak of WS_2 and we can see that both the peaks are independent of the crystal orientation and

follows the polarization of excitations. The E_{2g} and the PL intensities show a phase difference of 90°. The E_{2g} phonon mode switches the valley index of the photoexcited carrier while the luminescence photons have the same helicity as the incident photons.[105] Since a linearly polarized light can be represented as a coherent superposition of two circularly polarized light of opposite helicities, the phase difference is 90° for the linear polarization. Figure 9d-f also show the polarization dependence of graphene G peak for various samples grown at 900 °C.

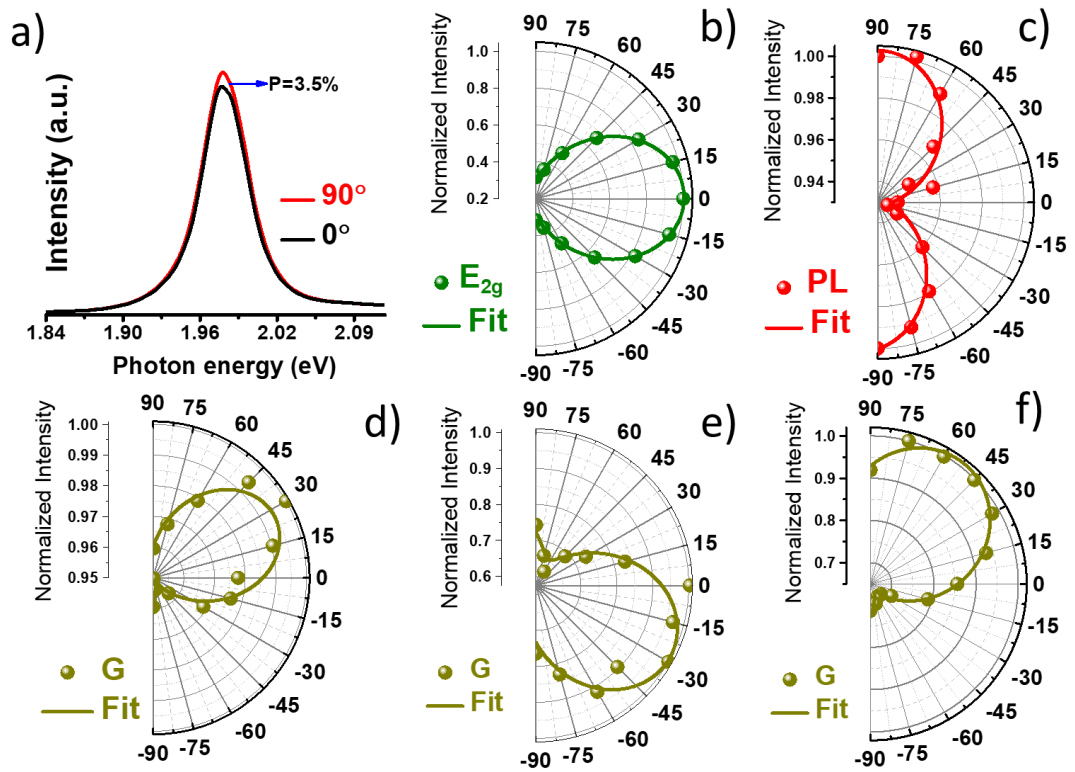

Figure 9: a) Photoluminescence spectra of WS_2 grown at 900° C at parallel and perpendicular polarization orientations. Polar plots for the intensities of the b) WS_2 E_{2g} and c) WS_2 photoluminescence peaks as a function of the polarization angle varied from -90° to 90°. d-f) Polar plots for graphene G peak intensities. The fits follow $\cos^2(\theta-\Phi)$ where θ is the polarization angle and Φ is the phase difference.

3.4 Conclusion

In conclusion we have selectively grown WS_2-graphene vertical heterostructures by controlling the growth temperature. By employing the technique of Raman spectroscopy and

analyzing the Raman and photoluminescence signature peaks, we have confirmed the selective growth of WS_2 on graphene at growth temperatures of 900 °C and 925 °C. At 950 °C, the growth of WS_2 on both graphene covered and uncovered SiO_2 regions can be explained in terms of lowering of the potential energy minima of the precursors adsorbing on the uncovered SiO_2 sites. The selectivity also resulted in the growth of WS_2 with spatially varying band gaps. The few layered WS_2 (~4 nm) on graphene have a lower band gap compared to the monolayer WS_2 on SiO_2. We have also performed linear-polarization resolved spectroscopy and presented the first report on polarization dependent Raman and photoluminescence spectra of WS_2 directly grown on graphene. This can pave the way to future electronic and optoelectronic devices harnessing the valley degree of freedom in heterostructures composed of WS_2, graphene and other 2D nanomaterials.

Chapter 4 WS_2-Induced Enhanced Optical Absorption and Efficiency in Graphene/Silicon Heterojunction Photovoltaic Cells

(Previously published as Debbarma, R.; Behura, S. K.; Wen, Y.; Che, S.; Berry, V. WS_2 - Induced Enhanced Optical Absorption and Efficiency in Graphene/Silicon Heterojunction Photovoltaic Cells. Nanoscale 2018, 10 (43), 20218–20225.)

The Van Hove singularity (VHS) induced enhancement of visible-frequency-absorption in atomically-thin two-dimensional (2D) crystals provides an opportunity for improved light management in photovoltaics; however, it requires the 2D nanomaterial to be in close vicinity to a photojunction. In this chapter, we present the design of a Schottky junction-based photovoltaic system with single-layer graphene atop *n*-type silicon (n-Si), which is interfaced directly with few-layers of tungsten disulfide (WS_2) *via* a bottom-up CVD synthesis strategy. An enhanced power conversion efficiency in the architecture of WS_2-graphene/*n*-Si is observed compared to graphene/*n*-Si. Here, the WS_2 induced photon absorption, only one atom above the photo-junction enhanced short-circuit current density (J_{SC}), and the reconfiguration of the energy band structure led effective built-in electric field induced charge carrier transport (enhanced open-circuit voltage (V_{OC})). Similar to graphene/*n*-Si Schottky junction, the WS_2-graphene/*n*-Si double junction exhibited non-linear current density-voltage (*J*-*V*) characteristics with a 4-fold increase in J_{SC} (2.28 mA/cm^2 in comparison to 0.52 mA/cm^2 for graphene/*n*-Si) and 40% increase in the V_{OC} (184 mV compared to 130 mV for graphene/*n*-Si) with a 6-fold increase in the solar cell power conversion efficiency. Futuristically, we envision an evolution in 2D heterojunctions with sharp-transitions in properties within a few nanometers enabling control on optical-absorption, carrier-distribution, and band-structure for applications including tandem photovoltaic cells and 2D optoelectronic circuit-switches.

4.1 Introduction

The abrupt gradients of optical and electronic properties within stacked van der Waals heterostructures of two-dimensional nanomaterials (2DNM) and heterojunctions of 2DNM and bulk crystals can be harnessed to achieve advanced functionalities.[24,28,43,91,106] The ultra-high charge carrier mobility and spectral transmittance of sp^2-hybridized graphene produced *via* catalytic chemical vapor deposition (CVD) process makes it an ideal candidate material for optoelectronic phenomena.[107–109] Typical CVD-produced graphene interfaced with lightly-doped silicon (*n*-Si) forms Schottky junction functioning as photovoltaic cells with illumination of light (air mass 1.5G).[110–112] Such heterojunctions show promising power conversion efficiency of >10% and further enhancement in the performance can be achieved by polymer doping of graphene with trifluoromethanesulfonic acid and also by using colloidal titanium dioxide layer as an antireflective coating.[113,114]

Atomically-thin transition metal dichalcogenides (TMDC) exhibit strong light-matter interactions due to the Van Hove singularities (VHS) in the electronic density of states.[35] The Van Hove singularities in the density of states of TMDC result in the sharp increase in the joint density of states in the visible region. This leads to an increased photo-absorption and electron-hole pair (exciton) generation in the visible range. In contrast, the Van Hove singularities in graphene's density of states lead to a pronounced absorption peak in the ultraviolet region.[115] Further, TMDC of thickness less than 1 nm can absorb up to 5-10% of incident sunlight compared to 2-3% absorption in monolayer CVD graphene.[116,117] They also possess a finite and tunable band gap (1.4-2.1 eV) in the visible region and therefore they can absorb a broad range of the solar radiation spectrum (air mass 1.5G). Tungsten disulfide (WS_2) is a member of the layered group-VI TMDC made up of covalently bonded S-W-S in-plane sheets held together *via* weak out-plane van der

Waals forces.[118] The energy bandgap for WS_2 transitions from an indirect bandgap of 1.4 eV in its bulk to a direct bandgap of 2.1 eV in its monolayer form.[119] The chemical stability and the presence of only a weak impurity band compared to molybdenum disulfide (MoS_2),[28] makes WS_2 better suited as an active absorber material for applications in photovoltaics as the lack of impurity bands will lead to fewer electron-hole pair recombination. The CVD growth of single crystalline grains and large area WS_2 has been reported in the literature.[20,120,121] CVD growth of TMDC allows for a better control of the number of layers and helps realize clean interfaces by avoiding the use of polymer-based transfer techniques. The direct growth of WS_2 and other TMDC *via* CVD will enable bulk production and eventually these 2DNM will find their way into commercial applications. A few reports have investigated utilizing WS_2 as a tunneling barrier in a graphene/WS_2/metal or graphene/WS_2/graphene vertical field-effect transistors using mechanically exfoliated WS_2 films.[28,93] In another report, CVD grown WS_2 were transferred onto CVD grown graphene to investigate the doping effect of WS_2 on graphene.[122]

In this chapter, we show (a) the direct CVD growth of WS_2 on graphene *via* bottom-up CVD synthesis strategy (shown for the first time), (b) the development of a double junction photovoltaic cell by vertically stacking WS_2 on graphene on *n*-type Si substrate, and (c) an enhanced power conversion efficiency in WS_2-graphene/*n*-Si photovoltaic solar cells over graphene/*n*-Si single Schottky junction solar cells. The mechanism of efficiency-enhancement is attributed to energy band restructuring, enhanced photon absorption, exciton generation and dissociation, and built-in electric field induced transport across the double junction.

4.2 Results and Discussion

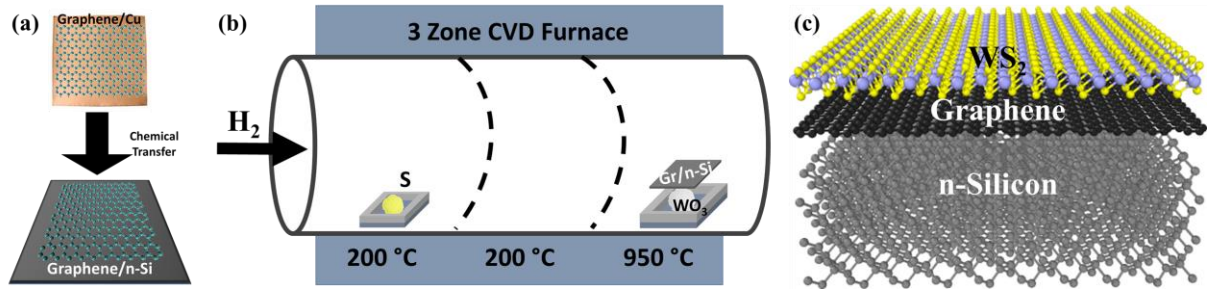

Figure 10: (a) Schematics of transfer of graphene from Cu foil onto *n*-Si substrate and (b) CVD synthesis of WS_2 on graphene/*n*-Si substrate. (c) Schematic of the stacked WS_2-graphene/*n*-Si heterojunction.

The bottom-up synthesis strategies for creating vertically-stacked WS_2-graphene/*n*-Si dual-junction nano-architecture is presented in Figure 10. Here a single-layer of CVD-produced graphene film on copper (Cu) foil is chemically transferred *via* carrier-film method onto a heavily-textured and lightly-doped solar-grade *n*-Si (100) substrate (Figure 10a) followed by the growth of atomically-thin WS_2 layers (Figure 10b) *via* vapor-transport based low-pressure thermal CVD technique.[123] As shown in Figure 10b, the WS_2-graphene/*n*-Si structures were prepared by growing WS_2 on the graphene/*n*-Si substrates in a three zone CVD furnace with a one inch quartz tube. The graphene/*n*-Si samples were inverted and placed on top of a crucible containing 10 mg of WO_3 powder at the third zone of the furnace and sulfur powder was kept in the first zone in a quartz boat. The CVD reaction chamber was vacuumed to 2 mTorr in 20 minutes and then a steady flow of 50 sccm of H_2 was maintained throughout the process. After a pressure of 220 mTorr was stabilized, the first and the second zones were heated to 200 °C and the third zone was heated to 950 °C in 30 minutes. The temperatures in all the three zones were held for the next 30 minutes. After 30 minutes, the chamber was cooled down to 700 °C at the rate of ~2 °C/min. This was followed by fast cooling (~100 °C/min) of the chamber to room temperature. Details of the CVD synthesis of graphene on catalytic Cu foil, its chemical transfer onto n-Si substrates are provided in the Materials and Methods section. Here ten different WS_2-graphene/*n*-Si samples were

produces *via* the CVD process. The synthesized vertically stacked heterojunction of WS_2-graphene/*n*-Si (Figure 10c) is elucidated by Raman spectroscopy. The spectrum for the stacked heterojunction shown in Figure 11a exhibits the signature Raman vibrational modes for WS_2 (in-plane E_{2g}/347 cm^{-1} and out-plane A_{1g}/415 cm^{-1})[124] and graphene (D/1352 cm^{-1}, G/1584 cm^{-1} and 2D/2700 cm^{-1})[125] as well as the photoluminescence (PL) peak for WS_2 (2344 cm^{-1} or 2.04 eV). The presence of PL peak and a peak difference of 68 cm^{-1} between the E_{2g} and A_{1g} peaks indicate that the WS_2 film grown on the graphene/*n*-Si substrate is few-layers thick and not bulk.[20,126] The presence of semi-metal graphene quenches the strong PL of WS_2.[99] Figure 11b shows the spatial mapping of the intensity of WS_2's E_{2g} peak, which represents the in-plane phonon mode involving the vibration of the metal (W) and the chalcogen (S) atoms.[105] The spatial mapping of the intensity of the graphene's G band (~1600 cm^{-1}), which represents the phonon mode for the in-plane stretching of carbon-carbon bond,[127] is shown in Figure 11c. A continuous coverage of WS_2 layer on the graphene transferred onto the *n*-Si substrate can be confirmed from the spatial mappings in Figure 11b and c. The variation in intensities in the spatial mapping is due to the surface texture of the underlying *n*-Si substrate, which is intentionally made on the *n*-Si substrate for enhanced light absorption.[128] Because of the surface texturing, some portion of the scanned area are above or below the focal plane used in the Raman measurement which ultimately leads to the variations in the intensities. The surface texture can also be seen in the micrographs and atomic force microscopy topography image for the WS_2-graphene/*n*-Si device shown in Figure 11d-f.

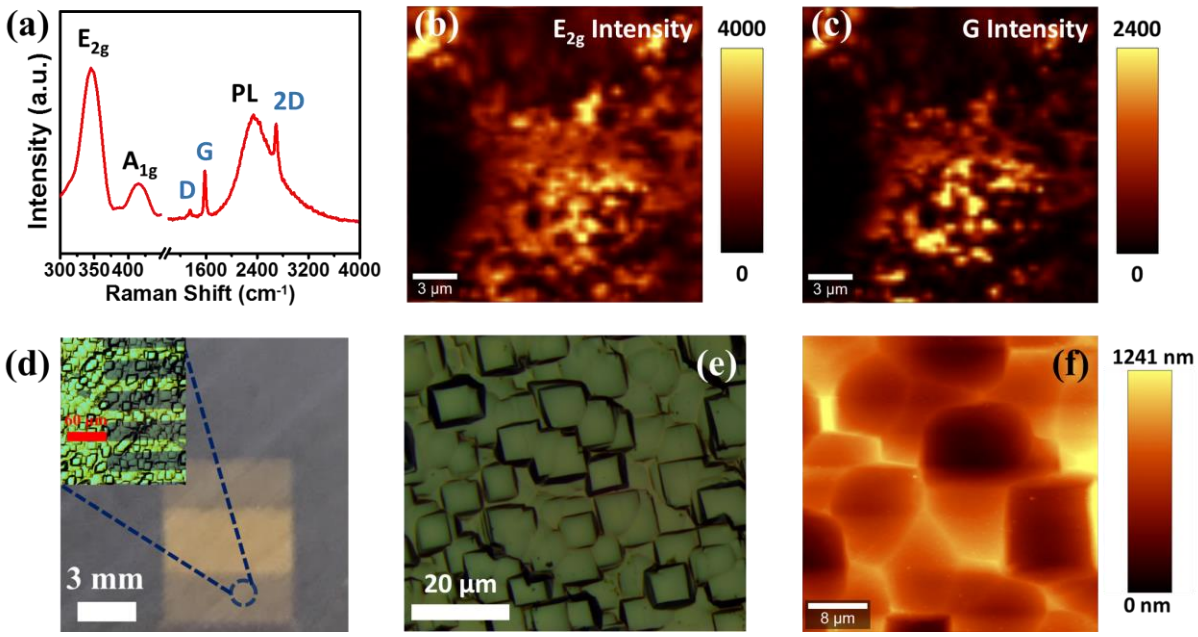

Figure 11: (a) Raman spectra of the stacked 2D heterojunction showing the characteristic Raman vibrational bands for WS_2 (E_{2g} and A_{1g}) and for graphene (D, G and 2D) and the photoluminescence peak of WS_2 at 2344 cm^{-1} (2.04 eV). Spatial intensity Raman mapping for WS_2's E_{2g}-band (b) and graphene's G-band (c), respectively. Optical micrographs of WS_2-graphene/*n*-Si device (d) and WS_2 film on graphene/*n*-Si surfaces (e). (f) AFM topography image for the WS_2-graphene/*n*-Si heterostructure.

Figure 12a and b show the dark current-voltage (*I-V*) characteristics of the graphene/*n*-Si and WS_2-graphene/*n*-Si heterojunction devices, respectively. Both devices have an active area of 0.1 cm^2. The *I-V* curves show non-linear diodic features for both the heterojunctions. The typical dark *I-V* relation[111,129] for a diode is given by:

$$I = I_O\left(exp\left(\frac{V-IR_s}{nV_T}\right) - 1\right) \qquad (1)$$

where I_O is the reverse saturation current, R_s is the series resistance, n is the diode ideality factor and V_T is the thermal voltage ($V_T = \frac{k_B T}{q}$). The diode equation is generally for a single *p-n* junction diode. In our case, even though we have a double junction structure (WS_2-graphene/*n*-Si), the electron transport occurs from WS_2 to graphene and then to *n*-Si (explained later) and so we can model the device as a single *p-n* junction diode and analyze the aforementioned parameters. The

diode parameters for the dark *I-V* relation were determined by employing a non-linear implicit curve fitting. The ideality factors determined from the non-linear implicit fitting of the *I-V* curves are 2.78 and 20.6 for the graphene/*n*-Si and the WS_2-graphene/*n*-Si devices, respectively. A previous work involving gallium nitride (GaN) based heterojunction reported anomalously high ideality factors.[130] It has been shown that the rectification of the individual junctions in the heterojunction can lead to high ideality factors and the measured ideality factor is the sum total of the ideality factors of the individual junctions. Here both the WS_2/graphene and graphene/*n*-Si junctions in the WS_2-graphene/*n*-Si structure contribute to the high ideality factor compared to just the one junction in the graphene/*n*-Si device.

The diode and photovoltaic parameters outlined in Table 1 shows that the addition of a thin film of WS_2 on graphene/*n*-Si structure leads to a four-fold increase in the short-circuit current density (J_{sc}) and the open-circuit voltage (V_{oc}) increases by 40%. This leads to a 6-fold improvement of the solar cell power conversion efficiency (η) from 0.015% to 0.1% *via* inclusion of a few layers of WS_2 on graphene/n-Si. The kink in the *J-V* curve (Figure 12c) can be attributed to the native oxide layer on the *n*-Si surface, which leads to an increased recombination current.[111] This results in low fill factors of 21% and 21.35% for the graphene/*n*-Si and the WS_2-graphene/*n*-Si devices, respectively. The large active area can also be attributed to the low fill factor and the high series resistance values obtained, which contributes to the low efficiencies observed in our solar cell devices.[114] A further improvement in the performance of the WS_2-graphene/*n*-Si device can be achieved *via* (a) chemical or physical doping, (b) plasmonic enhancement *via* nanoparticle anchoring, (c) anti-reflection coating for improved light management, (d) improving isolation of electrodes, and (e) maximizing the optical absorption *via* the optimization of the number of WS_2

layers. To understand the increases in the short circuit current density and the open circuit voltage, we need to look into the electrostatics and energetics of the photo-junction interfaces.

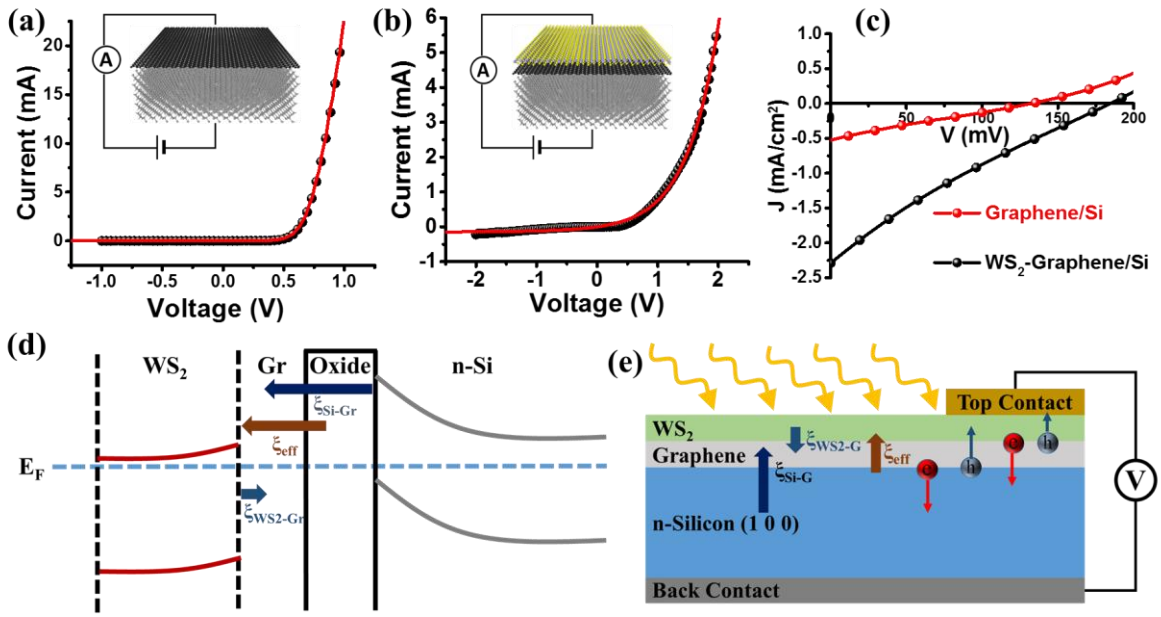

Figure 12: Dark condition current-voltage characteristic curves for (a) graphene/*n*-Si and (b) WS_2-graphene/*n*-Si junctions. The black dots show the data points and the red curves represent the fit of the non-linear diode equation. (c) Light condition current density-voltage characteristics under AM 1.5G illumination. (d) Schematic of the energy band structure for the stacked heterostructure. (e) Schematic representation of the photo-generation of the excitons and the separation of electron and hole pairs because of the effective built-in electric field along the direction of the WS_2 layer.

The deposition of *n*-type WS_2 layers on graphene/*n*-Si leads to the formation of a double junction photovoltaic cell. Unlike a single *p*-*n* junction where electron transport is from the *p*-side to the *n*-side upon light absorption with photon energy higher than the bandgap of the junction material, the transport of electrons in the WS_2-graphene/*n*-Si is from the *n*-type WS_2 to *p*-type graphene and then to the *n*-Si side. This can be attributed to the stronger built-in electric field in the graphene/*n*-Si interface (ξ_{Si-G}) compared to the WS_2-graphene interface (ξ_{WS_2-G}) as represented in Figure 12d and e. The electric field in the depletion region is directly proportional to the doping density and inversely proportional to the permittivity of the material. The built-in

electric fields at the WS_2-graphene and graphene/*n*-Si interfaces can be modelled using the following equations,

$$\xi_{WS_2-G}(x) \approx \frac{qN_D(x-W_n)}{\varepsilon_{WS_2}\varepsilon_o} \quad (2)$$

$$\xi_{Si-G}(x) \approx \frac{qN_D(x-W_n)}{\varepsilon_{Si}\varepsilon_o}, \quad (3)$$

where x is the distance from the given interface, q $(1.6 \times 10^{-19}\ C)$ is the elementary charge, N_D is the intrinsic dopant concentration $(N_D[Si] \approx 10^{18}\ cm^{-3})$, W_n is the depletion region width, $\varepsilon_{WS_2} = 4.4 - 11.5$ (monolayer to bulk)[131] and $\varepsilon_{Si} = 11.68$ are the relative dielectric constants and ε_o $(\varepsilon_o = 8.85 \times 10^{-12}\ F/m)$ is the vacuum permittivity. The intrinsic doping concentration for WS_2 can be written as $N_D = \frac{N_s}{t}$ where N_S $(N_S \approx 10^9\ cm^{-2})$ is the surface doping density and t is the WS_2 thickness.[132] The maximum electric field for both the junctions will be at the interface $(x = 0)$. The WS_2-graphene forms an abrupt 2D junction with no inter-diffusion and depletion region. In equation 2, the width of the depletion layer can be replaced by the thickness of the WS_2 layer, t. The depletion region width for the silicon-graphene junction is can be expressed as:[133],

$$W_n = \sqrt{\frac{2\varepsilon_{Si}\varepsilon_o(V_{bi}-V_b)}{qN_D}}, \quad (4)$$

where V_{bi} and V_b are the built-in and applied bias voltages, respectively. For V_{bi} = 0.5 V and V_b = 0 V, the depletion region width is $(W_n) \approx 0.01\ \mu m$. Performing an order of magnitude analysis, we can show that $\left|\xi_{WS_2-G}(x=0)\right| \approx 10^4\ V/m$ and $|\xi_{Si-G}(x=0)| \approx 10^7\ V/m$ and so the electric field along the silicon-graphene direction is three orders of magnitude higher $\left(\frac{|\xi_{Si-G}(x=0)|}{|\xi_{WS_2-G}(x=0)|} \approx\right.$

$10^3\Big)$ than the electric field along the WS_2-graphene direction. As mentioned earlier, the presence of native oxide layer on the *n*-Si surface leads to a low fill factor of ~20%. This native oxide layer will also shield and make the net electric field weaker by a factor ($|\xi_{Si-G\ net}| = |\xi_{Si-G\ net}|/\varepsilon_{ox}$), which is the dielectric constant of the oxide layer (ε_{ox}). The oxide layer can be approximated to have the same dielectric constant as silicon dioxide ($\varepsilon_{ox} = 3.9$). Therefore, the net electric field along the silicon-graphene direction is still of the order of $10^6 - 10^7\ V/m$ and two to three orders of magnitude higher $\left(\frac{|\xi_{Si-G\ net}|}{|\xi_{WS_2-G}|} \approx 10^2 - 10^3\right)$ than the electric field in the WS_2→graphene direction. Once this electric field penetrates the WS_2 layer, it is further weakened by a factor given by the dielectric constant of WS_2 (ε_{WS_2}). Since WS_2 has a low dielectric constant, the net effective field $\xi_{Si-G\ net}$ in the WS_2 layers is still two to three orders of magnitude higher than ξ_{WS_2-G}. Therefore, despite the shielding of the electric field by the native oxide layer and the opposing electric field in the WS_2→graphene direction, the relatively strong electric field in the *n*-Si→graphene interface penetrates the atomically thin WS_2-graphene junction, and that leads to an effective electric field along the *n*-Si→WS_2 direction. The effective field will drift the electrons towards *n*-Si and holes in the opposite direction towards WS_2.

Table 1: Diode equation parameters, short circuit current density, open circuit voltage, fill factors and the solar cell power conversion efficiencies for the two photovoltaic cells.

Photovoltaic Parameters	**Graphene/*n*-Si**	**WS_2-graphene/*n*-Si**
Dark Saturation Current, I_O *(μA)*	0.05	125
Series Resistance, R_s *(Ω)*	2.11	2.89
Ideality Factor, *n*	2.78	20.6
Short-Circuit Current, I_{sc} *(mA/cm²)*	0.52	2.28
Open-Circuit Voltage, V_{oc} *(mV)*	130	184

Fill Factor, *FF (%)*	21	21.3
Power Conversion Efficiency, *η (%)*	0.015	0.1

The native *n*-type doping of WS_2 similar to that in MoS_2 can be attributed to sulfur vacancies.[134,135] It has been reported that on transferring WS_2 layer onto graphene surface, the WS_2 becomes less *n*-doped and the underlying graphene covered by the WS_2 becomes less *p*-doped *via* exchange of electrons.[122] However, for the direct CVD grown WS_2 on graphene, we observed the opposite trend. A higher *n*-doping is seen on WS_2 grown on graphene/*n*-Si compared to the WS_2 grown on SiO_2/Si surface. The increase in the doping level of WS_2 can be seen in the PL spectra shown in Figure 13a and b. The PL spectra for WS_2 on SiO_2 and on graphene/*n*-Si in Figure 13a and b have been deconvoluted using Lorentzian fitting into two different peaks representing the exciton emission (X) and the trion emission (X^-).[136,137] The PL of WS_2 on graphene/*n*-Si shows a third peak that can be attributed to the 2D Raman vibrational mode for graphene. The blue-shift in the peak energy for the WS_2 on graphene compared to WS_2 on SiO_2 can be attributed to the structural imperfections and *n*-doping.[138] The two peaks (X and X^-) have an energy difference of 21.67 meV for WS_2 on graphene/*n*-Si and 25.55 meV for WS_2 on SiO_2 which is the sum of the trion binding energy and the fermi energy.[139–142] The intensity ratio of the trion emission peak to the exciton emission peak is higher for the WS_2 on graphene/*n*-Si$\left(\frac{I_{X^-}}{I_X} = 1.1\right)$ compared to that of WS_2 on SiO_2/Si $\left(\frac{I_{X^-}}{I_X} = 0.49\right)$ substrate. Further analysis is required to understand the increased trion concentration in direct growth of WS_2 on graphene. Although the PL analysis is not enough to confirm the doping effects on WS_2, the PL deconvolution and analysis does let us infer the ratio of trions to neutral excitons in the given system, which can be an indirect way of inferring the doping effect. The net negative charge of trions will aid in their drift under the effective in-built electric field towards the WS_2-graphene interface where they will dissociate into electrons and

holes. The neutral excitons, due to the chemical potential difference, will diffuse both towards and away from the interface and they will eventually dissociate at the WS_2-graphene interface.

The open-circuit voltage (V_{oc}) of a solar cell is directly dependent on the built-in potential and parameters that affect the built-in voltage.[143] In the WS_2-graphene/*n*-Si device both the WS_2/graphene and graphene/*n*-Si junctions have built-in voltages that contribute to the V_{oc} of the device. In multi-junction solar cell devices, the V_{oc} increases with the number of additional junctions. It has been shown that the V_{oc} in multi-cell (tandem junctions) devices is close to the sum of the V_{oc} of single cells.[144–147] So the V_{oc} in the WS_2-graphene/*n*-Si device is the sum of the V_{oc} for WS_2-graphene and graphene/*n*-Si single junction devices. The presence of an extra junction in the WS_2-graphene/*n*-Si device leads to the increase in the V_{oc}.

The increase in the short circuit current density (J_{sc}) can be attributed to the higher light absorption coefficient of WS_2 compared to graphene.[35,116] The Van Hove singularities in the density of states of WS_2 leads to sharp increase in the joint density of states in the visible region (~2-3 eV) which ultimately corresponds to the improved photo-absorption and generation of excitons. In comparison, the Van Hove singularities in graphene results in the absorption peaks in the ultraviolet (UV) range. A 3-fold increase in the absorption in the visible range on deposition of WS_2 on top of graphene is observed as exhibited by the absorption spectra in Figure 13c. The absorption for graphene exhibits a rapid reduction going from 300 nm to 400 nm (UV to visible range) compared to the slow reduction in the absorption for WS_2-graphene. The spectra for WS_2-graphene is more uniform in the wavelength range (300-900 nm) tested. The external quantum efficiency (EQE) in Figure 13d shows a low efficiency (10-20%) in the blue and green spectrum of light and a higher efficiency (~50%) in the near infrared region. The low EQE in the blue end of the light spectrum can be because of the carriers generated close to the front surface being

affected by the higher rate of recombination in the front region. The low EQE in the green region can be due to the low diffusion length or high bulk recombination rates that affects the collection probability from the bulk of the solar cell. The higher EQE in the near IR region can be attributed to the ability of charge carriers being generated towards rear end of the device getting transported to the junction.[123]

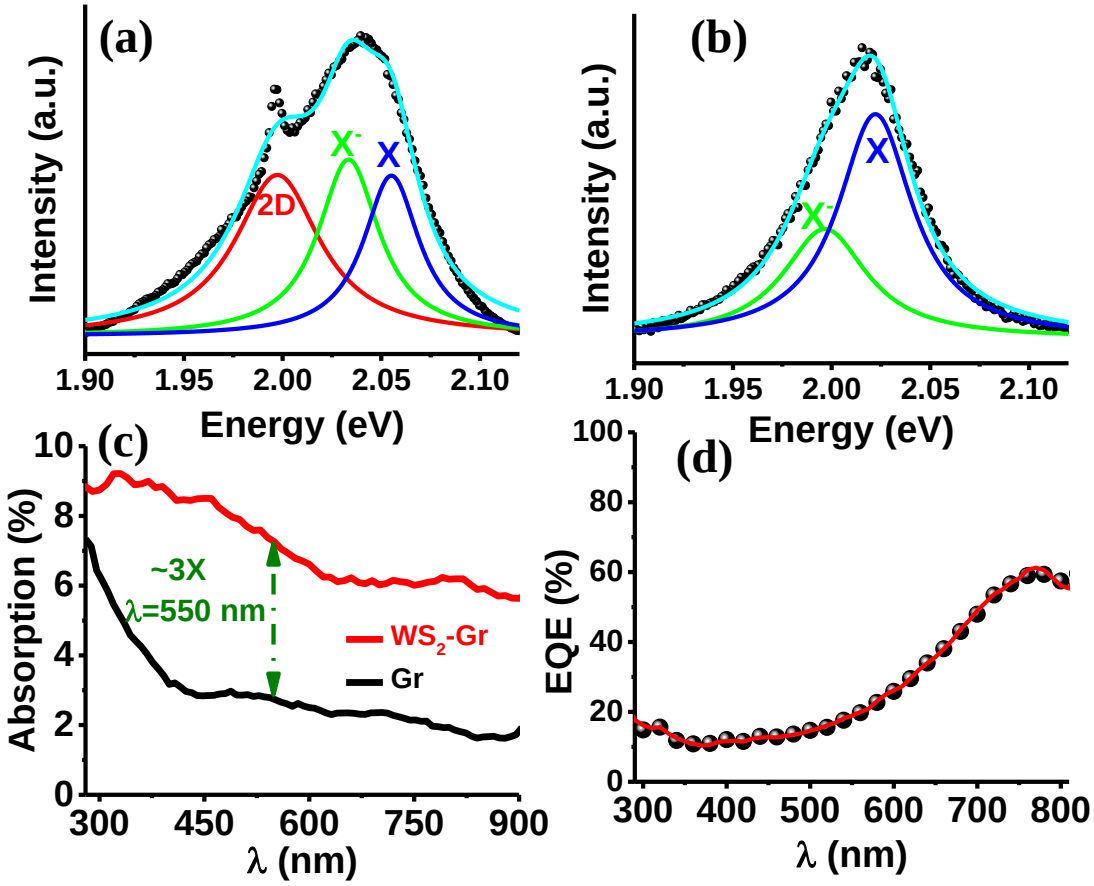

Figure 13: Photoluminescence spectra for WS_2 on (a) graphene/*n*-Si and on (b) SiO_2/Si surfaces. The Lorentzian fits show the neutral exciton (X) and the negatively charged trion (X^-) peaks for both the substrates. The PL spectrum for WS_2 on graphene/*n*-Si also exhibits the graphene's 2D Raman peak. (c) Absorption spectra for WS_2-graphene and graphene films showing an increased absorption in the WS_2-graphene film in the visible range. (d) External quantum efficiency for the WS_2-graphene/*n*-Si device.

Utilizing the Van Hove singularity induced absorption peaks in the visual and ultraviolet range of light, a 4-fold increase in the J_{sc} of the stacked heterostructure (WS_2-graphene/*n*-Si) has been achieved. Thus the deposition of a few layers of WS_2 on graphene/*n*-Si led to (a) an increased

light absorption leading to a 4-fold increase in the J_{sc} and (b) an increase in the V_{oc} by 40% due to the introduction of an additional photo-junction. In combination, a 6-fold increase in the solar power conversion efficiency of WS_2-graphene/*n*-Si double-junction photovoltaic cell is found in contrast to the graphene/*n*-Si single Schottky junction photovoltaic cell.

4.3 Conclusions

In this chapter, we reported the direct-CVD growth of atomically-thin semiconducting WS_2 layers on graphene and obtained a stacked WS_2-graphene/*n*-Si dual-junction heterostructure. Employing the technique of CVD we have been able to create a clean interface between WS_2 and graphene avoiding polymer based chemical transfer process. The CVD approach provides us avenues to control the number of layers of WS_2 and moreover this simple and fast process is also scalable. The stacked heterostructure helped in realizing atomically sharp interfaces. This abrupt change within a few angstrom distances helps in realizing sharp interfaces without inter-diffusion. As a consequence of the atomically thin WS_2-graphene interface and the stronger built-in electric field in the graphene/*n*-Si junction, the net built-in electric field is towards WS_2. Because of the net electric field, the photo-generated electrons will move toward the *n*-Si side and the holes toward WS_2 to be eventually collected by the metal electrodes on top. We leveraged the Van Hove singularity induced improved optical absorption of WS_2 in the visible range to enhance the light absorption of the graphene/*n*-Si device *via* deposition of few layers of WS_2. By synthesizing the stacked heterostructure, we have shown an improvement in the photovoltaic performance of a graphene/*n*-Si solar cell by depositing few-layers of WS_2 *via* CVD. Hence the improvement in the photovoltaic performance can be attributed to the increased light absorption and the reconfiguration of the energy levels at the WS_2/graphene junction as a consequence of the deposition of WS_2 layers on the graphene/*n*-Si substrate. The realization of stacked heterojunctions

via CVD will pave the way for future integrated nanostructures with unique optoelectronic functionalities.

4.4 Materials and Methods

4.4.1 Synthesis of Graphene on copper foil *via* chemical vapor deposition

The monolayer graphene samples were prepared *via* chemical vapor deposition (CVD) on a (1″x2″) copper foil (25 μm, 99.98% purity) with methane (CH_4, 99.95% purity, Praxair) as the precursor gas and hydrogen (H_2, 99.9999% purity, Praxair) gas as the reducing agent. The wash cycle of copper foil involved washing with copious amount of water followed by acetone and then isopropyl alcohol. After the first wash the copper foil was immersed in a solution of $Fe(NO_3)_2$:HNO_3 (1 M:3 M) for 10 minutes to remove native oxide. This was followed by a second wash cycle and then sonication in acetone to remove further ions. The third and final wash cycle was followed by drying with a flow of purified air for 2 minutes. The copper foil was subsequently loaded into a one-inch quartz tube on a single heating zone CVD furnace and the reaction chamber was vacuumed to a pressure of 1 militorr (mTorr) in 5 minutes. A steady flow of 100 sccm of H_2 gas was maintained throughout the rest of the synthesis process. After flushing the system with H_2 gas for 10 minutes, the temperature of the furnace was raised to 1050 °C in 15 minutes. This was followed by annealing the Cu foil at 1050 °C for 30 minutes. The reaction was carried out by flowing 10 sccm of CH_4 into the chamber for 1 minute. Subsequently, the CH_4 was turned off and the furnace was opened and allowed to cool down to room temperature quickly.

4.4.2 Transfer of graphene onto *n*-Si substrates

The monolayer graphene produced was transferred to the *n*-Si substrates using polymethyl-methacrylate (PMMA). The procedure involved spin-coating a 25 mg/ml solution of PMMA (MW 996000, Sigma Aldrich) in anisole (99% purity, Acros Organics) onto the graphene containing Cu

foil. This was followed by air drying the PMMA-graphene/Cu foil for 5 minutes and then etching copper by floating the foil in a HNO_3 acid solution (1:3 volume ratio of HNO_3 to deionized water) for 1 hour. The floating PMMA-graphene was picked up using a quartz substrate and then transferred to a container with deionized water. This process was repeated twice to remove the ions. Eventually the PMMA-graphene samples were picked up using the target *n*-Si substrates. The PMMA-graphene-Si samples were left to air dry for 1-2 hours. The PMMA removal procedure involved baking the samples on a hot-plate at 60 °C for 20 minutes followed by immersing the sample in a container with acetone. The graphene-Si samples were further washed with acetone to remove any remaining PMMA on the surface.

4.4.3 Photovoltaic device fabrication

To prepare the final solar cell devices a lift-off photolithography process was employed. Two out of the ten CVD prepared WS_2-graphene/*n*-Si samples produced were designed for photovoltaic cell architecture. The graphene/*n*-Si and WS_2-graphene/*n*-Si samples were first spin coated with a photoresist (PR OIR-90612) liquid followed by exposing it to ultraviolet (UV) light through a mask with our gridded electrode patterns. The samples were then developed by immersing the exposed samples in a developer solution (OPD 4262) for 1 minute which washed away the photoresist from the areas exposed to the UV light. The next step involved depositing the metal electrodes, 10 nm of chromium followed by 50 nm of gold, *via* electron-beam evaporation. The samples with deposited metals then were washed with acetone to remove metal from the photoresist covered areas leaving behind a gridded electrode pattern. A coating of conducting silver paste was used as the back contact for the solar cell devices.

4.4.4 Raman spectroscopic characterization

The Raman spectroscopy analysis for the samples were done on WITEC-300RA Raman-AFM system using a 532-nm laser excitation source.

4.4.5 Atomic force microscopy

The AFM measurements were performed on the WITEC-300RA Raman-AFM system. Tapping mode AFM was performed using silicon tips with a spring constant of 3 N/m and a resonant frequency of 62 kHz.

4.4.6 Photovoltaic Measurements

The photo-electrical measurements on the final devices were performed on a Keithley SMU 2612 source meter using the two-probe method. The photovoltaic effect of the devices was analyzed by measuring the *I-V* characteristics on the Keithley source meter under irradiation of AM 1.5 illumination from a solar simulator (Sciencetech).

4.4.7 Absorption Spectra and External Quantum Efficiency Measurements

The measurements were performed on the Oriel Cornerstone 130 monochromator system. To measure the absorption percentage, graphene film with and without WS_2 were transferred onto clean quartz slides. Using the monochromator, light from UV and visible range (280-900 nm) was irradiated onto the samples. The intensity of light transmitted through the samples were measured using a photodetector (Newport UV-818). The intensity of transmitted light through an empty quartz slide was used as the base intensity used in calculating the percentage absorption through the graphene and WS_2-graphene samples. The EQE measurement involved irradiating the fabricated device with light of different wavelengths using the monochromator and measuring the corresponding photocurrent through the Keithley SMU 2612 source meter.

Chapter 5 Temperature and Gate Dependent Photo-response and Valley Coherence in MoS_2-WS_2 heterostructure

Van der Waals heterostructures fabricated from different transition metal dichalcogenides can leverage the atomically sharp interfaces between various materials for ultrafast charge transfer between the layers which has various optoelectronic applications. In this chapter, we present vertical and lateral heterostructures of two structurally and electronically similar transition metal dichalcogenides, WS_2 and MoS_2, produced *via* chemical vapor deposition. A strong gate and temperature dependent photo-response was observed in field effect transistor devices fabricated using the MoS_2/WS_2 heterostructure as the channel material. It was observed that the photo-response decreased with increasing temperature and gate voltage. 2D variable range hopping (VRH) transport mechanism through the channel was determined *via* temperature-controlled conductivity measurements. Furthermore, valley coherence between the electrons and holes in the K and K′ points of the Brillouin zone was observed in the mixed structure *via* linearly polarized photoluminescence. This study has future applications in various 2D semiconducting electronic and optoelectronic devices.

5.1 Introduction

The presence of a finite band gap in various transition metal dichalcogenides (TMDC) make them ideal candidates for transistor materials and for various optoelectronic applications such as photovoltaic cells and light emitting devices.[34,36,148] Molybdenum and tungsten disulphide (MoS_2 and WS_2) are group VI TMDC with band gaps in the range of 1-2 eV that transitions from a direct to indirect as we go from monolayer to bulk.[19,20] The ultrafast charge transfer at the atomically sharp interfaces between MoS_2 and WS_2 make their heterostructures ideal for various optoelectronic applications.[30]

In monolayer TMDC the lack of inversion symmetry coupled with the time reversal symmetry gives rise to magnetic moment (m) and Berry curvature of equal magnitude and opposite signs at the K and K′ points of the Brillouin zone.[100] This inversion symmetry breaking leads to valley contrasted optical selection rule for interband transitions. Valleytronics is the field of electronics where the valley degree of freedom of an electron is used instead of charge or spin. Valley represents the maxima or minima point in the electronic band structure of a material. The valley degree of freedom can be used to store information. Electrons in degenerate valleys that can be manipulated to encode and store information are ideal for valleytronic applications. Strain and magnetic field can be used to manipulate the valley DOF. In graphene and other hexagonal 2D materials like TMDC, two inequivalent valleys occur at K and K′ points of the Brillouin zone. In TMDC along with spin-orbit coupling, the spin and valley are also coupled giving rise to the possibility of manipulating spin by utilizing the valley properties. In comparison to graphene and hBN, TMDC have a broken inversion symmetry because of the out of plane S atoms. This gives rise to valley dependent optical selection rules. Right hand circularly polarized light (RHC) gets coupled to the inter-band transitions in the K valley and LHC to the K′ valley. Circularly polarized light can be used to selectively populate the valleys with excitons. The K and K′ points of the Brillouin zone in TMDs have a large separation in the momenta space and hence the valley indices are preserved in the presence of scatterings by smooth deformations and long wavelength phonons. The polarization is not affected in the presence of magnetic field and hence they're not because of spin-dependent optical selection rules.

In certain TMDC, when a linear light is incident on the material, they excite electrons from both the valleys as the light consists of both LHC and RHC polarized light. Once the excitons recombine, they release circularly polarized lights that combine to form a linearly polarized light

if they are coherent. And this coherence can be seen in the linear polarization of certain PL peak in the TMDC. The coherence of optically generated excitons in the K and K′ valleys with identical emission energies leads to the linear polarization of PL peaks.[101]

In this chapter we investigate the electrical and optical properties of CVD grown MoS_2/WS_2 mixed structures *via* polarized Raman and photoluminescence spectroscopy, AFM and temperature dependent electrical conduction measurements. We demonstrate the effect of temperature and gate voltage on the photo-response of the MoS_2/WS_2 FETs and show that the charge carrier transport *via* variable range hopping mechanism through the structure. We also show room temperature valley coherence in the mixed structure and show how it depends on the type of material present in a certain domain.

5.2 Results

5.2.1 Raman characterization

The optical image in Figure 14a shows a grain that resembles a triangle. The intensity spatial mapping shown in Figure 14b of the MoS_2 E_{2g} peak revealed that the triangular structure observed in Figure 14a is a MoS_2 grain. The intensity spatial mappings of MoS_2 E_{2g} and WS_2 E_{2g} peaks are respectively shown in Figure 14c and d and they represent the area marked by the rectangle in Figure 14a. The mappings show the presence of WS_2 triangular grains on top of the larger triangular MoS_2 grain. The bright regions in the MoS_2 E_{2g} mapping correspond to the WS_2 region except for the bright spot on top which is because of a fold in the MoS_2 grain (explained below). The intensity spatial mappings for the A and B photoluminescence peaks of MoS_2 are shown in Figure 14e and f respectively. The WS_2 covered regions exhibited lower A peak intensities but relatively higher B peak intensities. The PL spectra for the flat (monolayer) and

folded (bilayer) MoS_2 are shown in Figure 14g and the PL spectra for the WS_2/MoS_2 region is shown in Figure 14h.

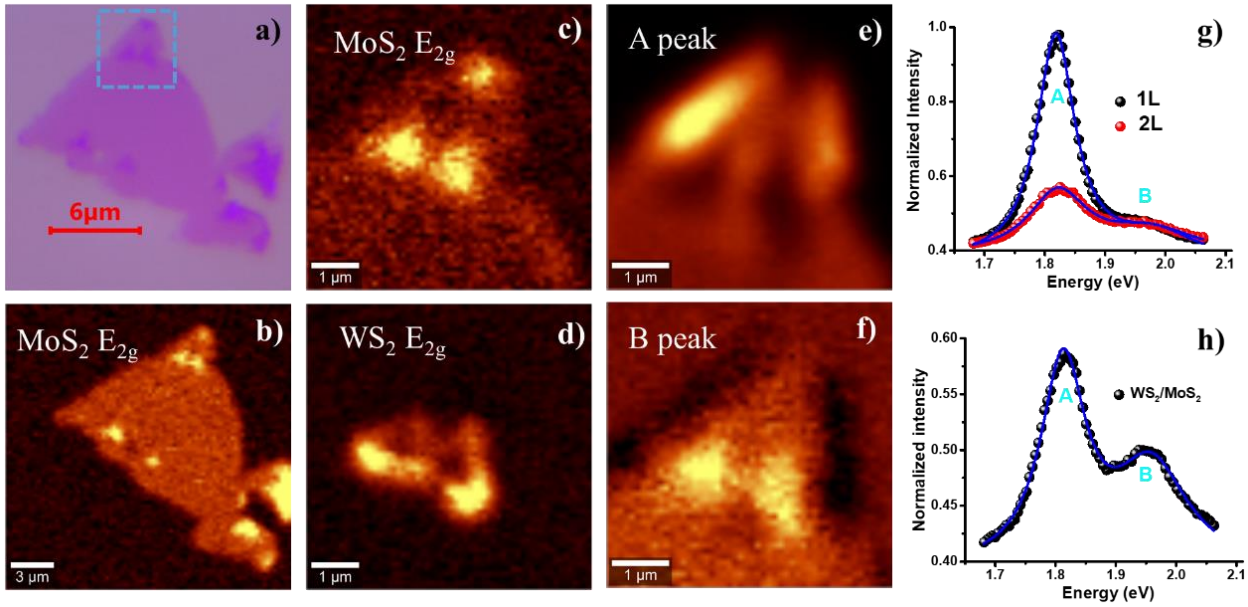

Figure 14: a) Optical micrograph for the CVD grown MoS_2/WS_2 grain. Raman and photoluminescence intensity mapping for b) & c) MoS_2 E_{2g}, d) WS_2 E_{2g}, e) A and f) B peaks. Photoluminescence spectra for g) monolayer and bilayer MoS_2 and h) WS_2 on MoS_2.

The spatial mappings of the A_{1g} and E_{2g} peak positions and the peak difference are shown in Figure 15a, b and c respectively. The A_{1g} peak for MoS_2 displays a blue shift in the regions covered by WS_2 and in the folded bilayer MoS_2 area compared to the monolayer regions. And a red shift in the MoS_2 E_{2g} peak is seen in the region covered by WS_2. The blue shift or the phonon stiffening observed in the A_{1g} peak of MoS_2 is observed in the presence of additional layers because of the suppression of the atomic vibrations.[149] The red shift in the E_{2g} peak is explained by the Coulombic screening because of the addition of extra layers. The same explanation can be used for the shifts in the MoS_2 peaks in the regions covered by WS_2.

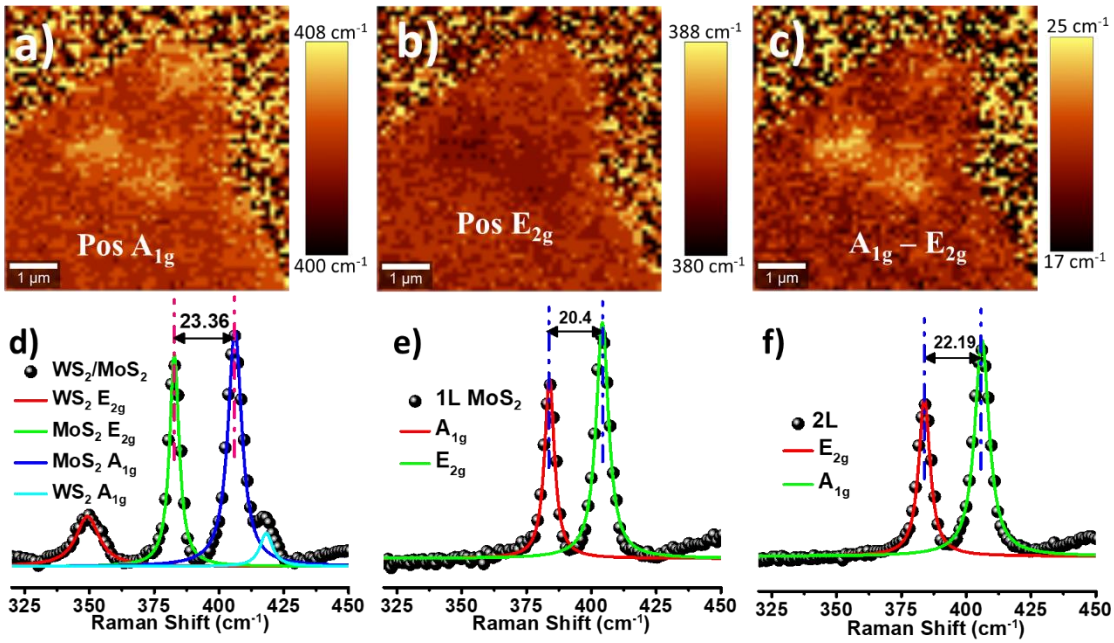

Figure 15: Raman position mapping of MoS_2 a) A_{1g} and b) E_{2g} peaks and c) their difference. The difference is higher in the folded bilayer MoS_2 and WS_2/MoS_2 regions. Raman spectra for d) WS_2/MoS_2, e) monolayer MoS_2 and f) folded bilayer MoS_2 regions.

5.2.2 AFM characterization

The structural characterization is obtained *via* tapping mode atomic force microscopy. The height profile along the folded MoS_2 and WS_2 (Figure 16c and f) regions confirm that the folded MoS_2 and WS_2 are single layers on top of the monolayer MoS_2 grain.

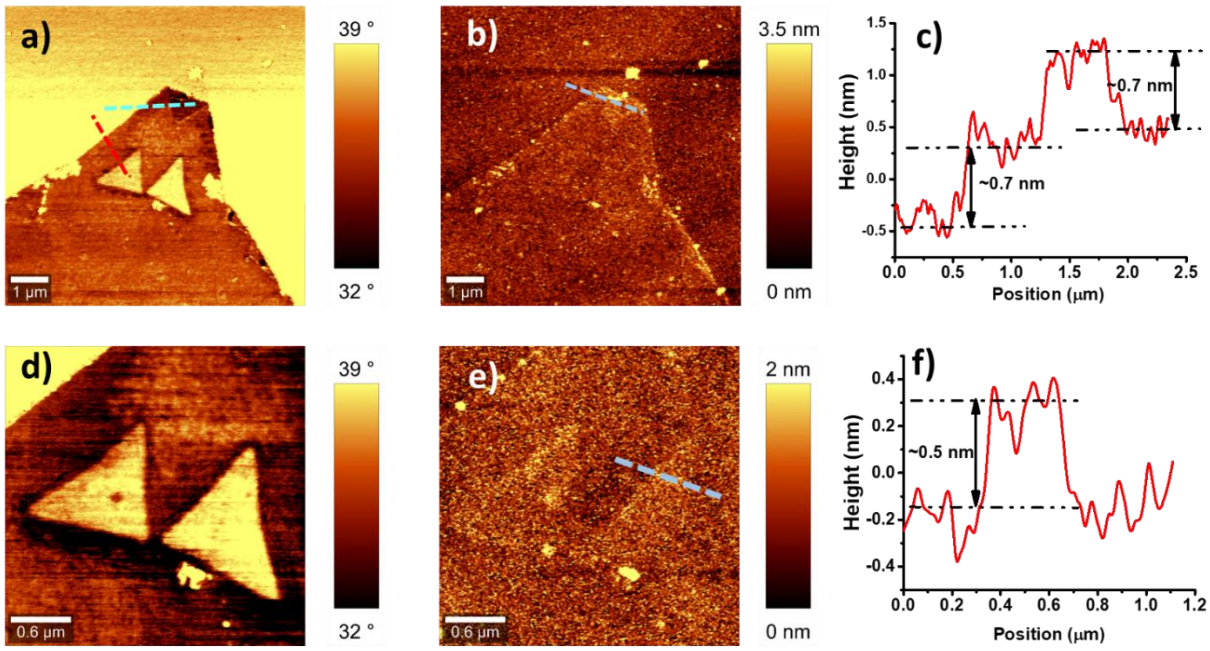

Figure 16: AFM phase a) & d) and topography b) & d) images for the MoS_2/WS_2 heterostructure. Height profile for c) monolayer and folded bilayer MoS_2 on SiO_2 and f) monolayer WS_2 on MoS_2

The phase differences in the phase image represents the phase shift recorded in the tapping mode AFM. The phase shift is sensitive to various surface characteristics like composition, adhesion, friction, viscoelasticity and topometric differences.[150] Since we're not dealing with soft materials and the topography exhibited no considerable difference in the slopes for the MoS_2 and WS_2 areas, we can rule out viscoelasticity and topometric differences as possible causes for the phase contrast observed. Phase shift is also a measure of the energy dissipation involved because of the interaction between the tip and the surface. The total energy dissipation is a sum of contributions from energy dissipated by the cantilever and the tip. The cantilever dissipation because of air damping is modelled by viscous damping. The relationship between the phase shift angle and the energy dissipated because of tip-sample interaction can be modelled by the formula

$$E_{dis} = \left(sin\phi - \frac{A}{A_0}\right)\frac{A}{A_0}\frac{\pi k A_0^2}{Q}$$

where ϕ is the phase shift, A and A_0 are the tapping and free amplitude, k is the spring constant and Q is the quality factor of the cantilever.[151,152] The above formula for dissipation is applicable when the cantilever is operated at the resonant frequency $(\omega = \omega_0)$.The formula above shows that for a constant amplitude the phase is a function of energy dissipated as a result of tip-sample interaction.

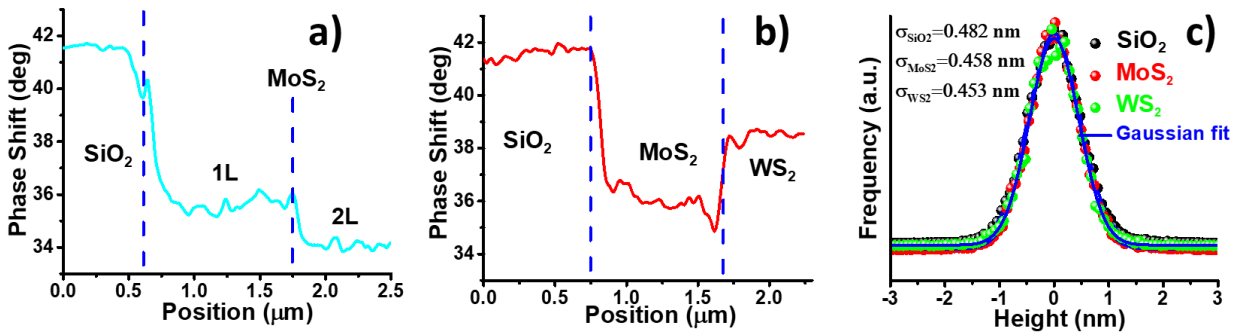

Figure 17: Phase profile plots for the a) blue and b) red dashed lines shown in figure 16a. c) Roughness histogram showing similar roughness for SiO_2, MoS_2 and WS_2.

The phase profiles in Figure 17a and b show a higher phase shift in the uncovered SiO_2 region compared to the MoS_2 region. And the phase shift in the bilayer MoS_2 and WS_2 regions are lower and higher than the phase shifts in the monolayer MoS_2 region respectively. Since the sine function is monotonically increasing from 0° to 90°, from the above equation we can conclude that the dissipated energy is the highest in uncovered SiO_2, followed by WS_2/MoS_2, monolayer MoS_2 and the lowest dissipation in bilayer MoS_2.

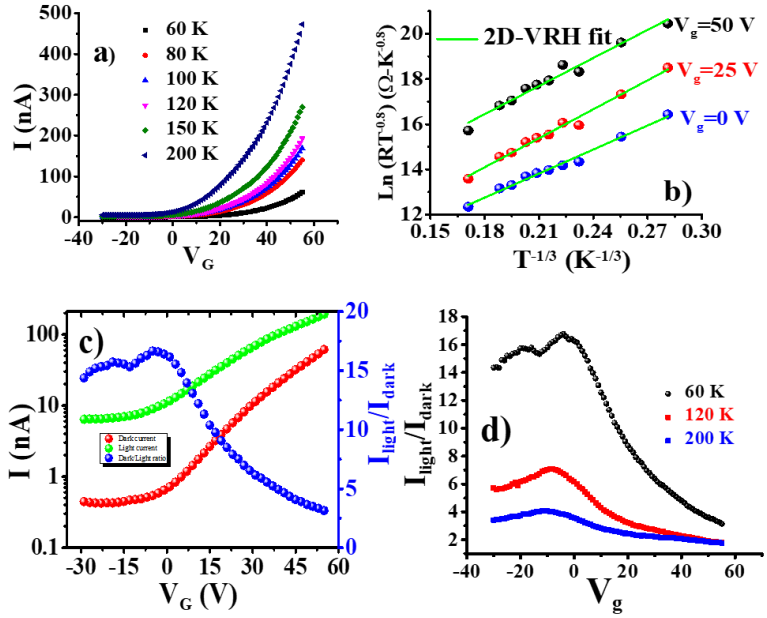

Figure 18: Electrical characterization of MoS_2-WS_2 heterostructure. a) The I_{DS}-V_G characteristic for the mixed structure at a bias voltage V_{DS}=5 V and different temperatures (60-200 K). b) The two-dimensional variable range hopping fit of the data obtained in a). c) Current and light response (I_{light}/I_{dark}) as a function of gate voltage at 60 K and d) light response at different temperatures for V_{DS}=5 V.

5.2.3 FET conduction mechanism

MoS_2-WS_2 heterostructure field effect transistor was fabricated by transferring the thin film grains onto printed gold electrodes. To elucidate the charge transport mechanism, the source-drain current at different gate voltages were obtained at cryogenic temperatures. The transfer curves (I_{DS}-V_G) shown in Figure 18a exhibit *n*-type characteristics. The conductivity increased with temperature as expected for a semiconductor type thin film. The temperature dependence of conductivity obtained fit with the 2D Mott variable range hopping model (Figure 18b). It has been shown that the presence of localized states because of substrate leads to 2D VRH hopping in MoS_2 devices.[153–155]

5.2.4 Light response

The light responses for the FET device exhibited temperature and gate voltage dependence as shown in Figure 18c and d. An overall trend of decreasing light response with increasing gate voltage and temperature was observed. This can be explained by the reduction in the number of energy states available in the conduction band as the number of electrons occupying the higher energy levels increases with temperature and gate voltage.

The light response curve also shows some peaks at negative gate voltages (lower charge carrier concentrations). This can be attributed to resonant tunneling transport. The transfer curves for the dark current shows oscillations at negative gate voltages while the current with light increases monotonically with increasing gate voltage.[153] Resonant tunneling has been mainly studied for 1-D double barrier cases.[156,157] It involves multiple reflections of electrons at the interfaces because of their wave nature. The reflections will interfere constructively at certain wavelength (energy) of the electrons and lead to a near-unity transmission probability. The phenomena of resonant tunneling can also be extended to 2D multiple barrier scenarios. Ghatak *et al.* reported oscillations in source-drain current with gate-voltage in CVD grown MoS_2 devices and attributed it to the influence of disordered localized states which are present because of the influence of the substrate.[153]

MoS_2-WS_2 hetero-bilayers exhibit type-II band alignment with the CB minima at the K points of MoS_2 and the VB maxima at the K or Γ points of WS_2.[158] In the mixed structure of our CVD grown films, the band misalignment can form double/multiple barrier systems which can also contribute to resonant tunneling.

In the light response curve shown in the Figure 18c, two peaks can be seen for 60 K and as the temperature was increased to 120 K, only one peak was observed. This can be attributed to the

broadening of the electron energy distribution at higher temperatures and the decrease in the electron concentration at the resonance energy.

5.2.5 Valley-coherence

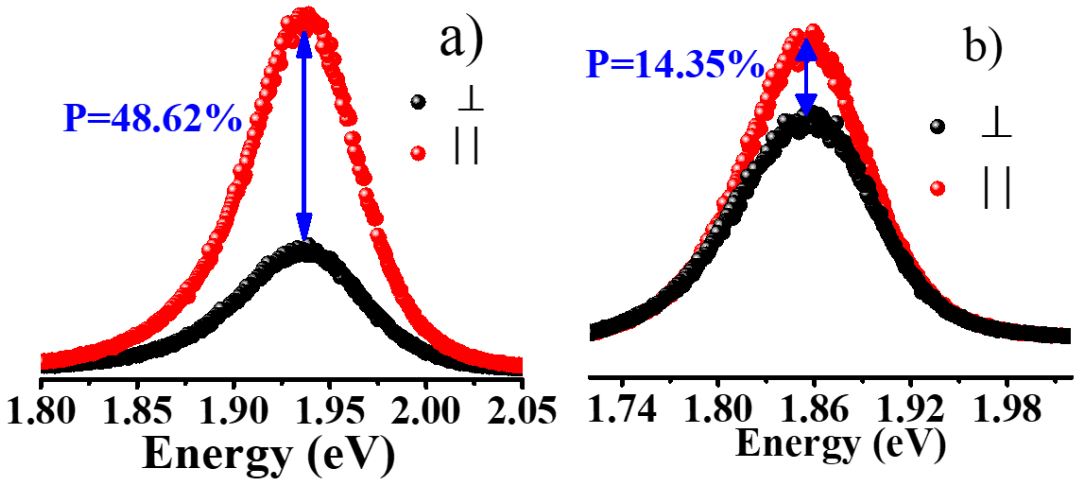

Figure 19: Linear polarization of PL peaks at a) WS_2 and b) MoS_2 domains in the mixed structure. The scattered light is passed through an analyzer that is parallel or perpendicular to the direction of the incident laser.

Figure 19 shows linear polarization of the photoluminescence of the mixed structure at two different spatial locations. This was obtained using a linearly polarized 532 nm light and measuring the scattered light parallel and perpendicular to the incident light. The PL energy for the WS_2 dominated region is around 1.94 eV whereas the MoS_2 dominated region exhibits a peak around 1.86 eV. The valley coherence in the mixed structure exhibited a higher degree of polarization in the WS_2 domain compared to the MoS_2 domain. This can be explained by the stronger spin-valley coupling strength in WS_2 of 0.4 eV compared to ~0.16 eV in MoS_2.[23,159] The stronger SOC in WS_2 is because the *5d* electron in W have a stronger magnetic moment and hence a stronger SOC compared to the *4d* electron in Mo.

5.3 Conclusion

In conclusion, mixed structures of MoS_2/WS_2 were grown *via* CVD and FET devices were fabricated to investigate their charge transport mechanism and study light response. The transfer curves show a *n*-type behavior for the mixed structure and a 2D VRH model of conduction was determined *via* temperature dependent conductivity studies. It was also observed that the light response of the FET has an inverse relation to temperature and gate voltage which is explained by the increased occupancy of available energy states in the conduction band at higher temperatures and gate voltages. Furthermore, we were able to achieve room temperature valley coherence of electrons and holes in the K and K′ valleys of the mixed structures observed through the linearly polarized photoluminescence peaks. Employing linearly polarized incident light, the valley coherence was observed to be higher in the WS_2 dominated domains compared to the MoS_2 domains which can be explained by the stronger spin orbit coupling strength of tungsten compared to molybdenum. We envision that this investigation on the optoelectronic and valley properties of photoluminescence will pave the way to futuristic valleytronic and quantum computing applications.

5.4 Materials and Methods

5.4.1 CVD growth

The growth of the heterostructure was carried out in a one-inch quartz tube inside a three-zone CVD furnace. The precursors were sulfur (Sigma-Aldrich, ≥ 99.5 %), molybdenum oxide (MoO_3, Sigma-Aldrich, 99.97% trace metal basis) and tungsten dioxide (WO_3, Sigma-Aldrich, 99% trace metal basis) powders. The sulfur powder (50 mg) was placed in the second zone on a glass boat while the MoO_3 (5 mg) and WO_3 (10 mg) powders were taken in an alumina crucible and placed on the third zone. The target substrate (SiO_2/Si) was placed upside down on top of the

crucible containing the metal oxides. The CVD growth was carried out at atmospheric pressure and 100 sccm of argon was flown through the chamber throughout the process. All the three zones were heated to 150 °C and held at that temperature for 20 minutes while maintaining an argon flow rate of 100 sscm. The temperatures are then ramped to 180 °C in the first two zones and 900 °C in the third zone in 30 minutes. The temperatures are then held for 30 minutes before the heating in the furnaces is turned off. The temperature of the third zone is allowed to slowly cool down to <700 °C with the furnace lid closed in about 10 minutes. This is followed by fast cooling to room temperature with the furnace lid open.

5.4.2 FET fabrication and characterization

The CVD grown MoS_2/WS_2 films were transferred onto Si chips with 300 nm of SiO_2 and printed gold electrodes top. The films on top of SiO_2 chips after the CVD growth were spin coat with PMMA and put in 2M KOH solution in water at 80 °C for approximately 30 minutes until the films were floating in the solution. The PMMA/MoS_2-WS_2 films were then transferred onto the printed electrodes and left to dry overnight. The PMMA was then removed in acetone bath at 60 °C and then the device was vacuum annealed at 200 °C for 4 hours in a tube furnace to remove the remaining PMMA and have a better contact between the film and the electrodes.

References

1 K. S. Novoselov, A. K. Geim, S. V. Morozov, D. Jiang, Y. Zhang, S. V. Dubonos, I. V. Grigorieva and A. A. Firsov, *Science (80-.).*, 2004, **306**, 666–669.

2 R. R. Nair, P. Blake, A. N. Grigorenko, K. S. Novoselov, T. J. Booth, T. Stauber, N. M. R. Peres and A. K. Geim, *Science (80-.).*, 2008, **320**, 1308 LP – 1308.

3 C. Lee, X. Wei, J. W. Kysar and J. Hone, *Science (80-.).*, 2008, **321**, 385–388.

4 A. A. Balandin, S. Ghosh, W. Bao, I. Calizo, D. Teweldebrhan, F. Miao and C. N. Lau, *Nano Lett.*, 2008, **8**, 902–907.

5 Y. B. Zhang, Y. W. Tan, H. L. Stormer and P. Kim, *Nature*, 2005, **438**, 201–204.

6 J. R. Williams, L. DiCarlo and C. M. Marcus, *Science (80-.).*, 2007, **317**, 638–641.

7 K. S. Novoselov, A. K. Geim, S. V. Morozov, D. Jiang, M. I. Katsnelson, I. V. Grigorieva, S. V. Dubonos and A. A. Firsov, *Nature*, 2005, **438**, 197–200.

8 G. Li, A. Luican, J. M. B. Lopes dos Santos, A. H. Castro Neto, A. Reina, J. Kong and E. Y. Andrei, *Nat. Phys.*, 2010, **6**, 109–113.

9 Y.-W. Son, M. L. Cohen and S. G. Louie, *Phys. Rev. Lett.*, 2006, **97**, 216803.

10 M. Y. Han, B. Özyilmaz, Y. Zhang and P. Kim, *Phys. Rev. Lett.*, 2007, **98**, 206805.

11 Y. Zhang, T.-T. Tang, C. Girit, Z. Hao, M. C. Martin, A. Zettl, M. F. Crommie, Y. R. Shen and F. Wang, *Nature*, 2009, **459**, 820–823.

12 M. A. Velasco-Soto, S. A. Pérez-García, J. Alvarez-Quintana, Y. Cao, L. Nyborg and L. Licea-Jiménez, *Carbon N. Y.*, 2015, **93**, 967–973.

13 Z. Pan, N. Liu, L. Fu and Z. Liu, *J. Am. Chem. Soc.*, 2011, **133**, 17578–17581.

14 K. Watanabe, T. Taniguchi and H. Kanda, *Nat. Mater.*, 2004, **3**, 404–409.

15 C. R. Dean, A. F. Young, I. Meric, C. Lee, L. Wang, S. Sorgenfrei, K. Watanabe, T. Taniguchi, P. Kim, K. L. Shepard and J. Hone, *Nat. Nanotechnol.*, 2010, **5**, 722–726.

16 Y. Kubota, K. Watanabe, O. Tsuda and T. Taniguchi, *Science (80-.).*, 2007, **317**, 932–934.

17 Q. H. Wang, K. Kalantar-Zadeh, A. Kis, J. N. Coleman and M. S. Strano, *Nat. Nanotechnol.*, 2012, **7**, 699–712.

18 H. S. S. Ramakrishna Matte, A. Gomathi, A. K. Manna, D. J. Late, R. Datta, S. K. Pati and C. N. R. Rao, *Angew. Chemie - Int. Ed.*, 2010, **49**, 4059–4062.

19 A. Splendiani, L. Sun, Y. Zhang, T. Li, J. Kim, C. Y. Chim, G. Galli and F. Wang, *Nano Lett.*, 2010, **10**, 1271–1275.

20 H. R. Gutierrez, N. Perea-Lopez, A. L. Elias, A. Berkdemir, B. Wang, R. Lv, F. Lopez-Urias, V. H. Crespi, H. Terrones and M. Terrones, *Nano Lett.*, 2012, **13**, 3447–3454.

21 K. F. Mak, K. He, J. Shan and T. F. Heinz, *Nat. Nanotechnol.*, 2012, **7**, 494–498.

22 H. Zeng, J. Dai, W. Yao, D. Xiao and X. Cui, *Nat. Nanotechnol.*, 2012, **7**, 490–493.

23 B. Zhu, H. Zeng, J. Dai, Z. Gong and X. Cui, *Proc. Natl. Acad. Sci.*, 2014, 1–6.

24 a K. Geim and I. V Grigorieva, *Nature*, 2013, **499**, 419–25.

25 M. Yankowitz, J. Xue, D. Cormode, J. D. Sanchez-Yamagishi, K. Watanabe, T. Taniguchi, P. Jarillo-Herrero, P. Jacquod and B. J. LeRoy, *Nat. Phys.*, 2012, **8**, 382–386.

26 A. S. Mayorov, R. V. Gorbachev, S. V. Morozov, L. Britnell, R. Jalil, L. A. Ponomarenko, P. Blake, K. S. Novoselov, K. Watanabe, T. Taniguchi and A. K. Geim, *Nano Lett.*, 2011, **11**, 2396–2399.

27 F. Amet, J. R. Williams, A. G. F. Garcia, M. Yankowitz, K. Watanabe, T. Taniguchi and D. Goldhaber-Gordon, *Phys. Rev. B - Condens. Matter Mater. Phys.*, 2012.

28 T. Georgiou, R. Jalil, B. D. Belle, L. Britnell, R. V Gorbachev, S. V Morozov, Y.-J. Kim, A. Gholinia, S. J. Haigh, O. Makarovsky, L. Eaves, L. a Ponomarenko, A. K. Geim, K. S. Novoselov and A. Mishchenko, *Nat. Nanotechnol.*, 2013, **8**, 100–3.

29 K. S. Novoselov, A. Mishchenko, A. Carvalho and A. H. Castro Neto, *Science (80-.).*, 2016, **353**, aac9439.

30 X. Hong, J. Kim, S.-F. Shi, Y. Zhang, C. Jin, Y. Sun, S. Tongay, J. Wu, Y. Zhang and F. Wang, *Nat. Nanotechnol.*, 2014, **9**, 682–686.

31 R. Cheng, D. Li, H. Zhou, C. Wang, A. Yin, S. Jiang, Y. Liu, Y. Chen, Y. Huang and X. Duan, *Nano Lett.*, 2014, **14**, 5590–5597.

32 F. Withers, O. Del Pozo-Zamudio, A. Mishchenko, a. P. Rooney, A. Gholinia, K. Watanabe, T. Taniguchi, S. J. Haigh, a. K. Geim, a. I. Tartakovskii and K. S. Novoselov, *Nat. Mater.*, 2015, **14**, 301–306.

33 M. M. Furchi, A. Pospischil, F. Libisch, J. Burgdörfer and T. Mueller, *Nano Lett.*, 2014, **14**, 4785–4791.

34 L. Ye, H. Li, Z. Chen and J. Xu, *ACS Photonics*, 2016, **3**, 692–699.

35 L. Britnell, R. M. Ribeiro, a Eckmann, R. Jalil, B. D. Belle, a Mishchenko, Y.-J. Kim, R. V Gorbachev, T. Georgiou, S. V Morozov, a N. Grigorenko, a K. Geim, C. Casiraghi, a H. Castro Neto and K. S. Novoselov, *Science*, 2013, **340**, 1311–4.

36 W. J. Yu, Y. Liu, H. Zhou, A. Yin, Z. Li, Y. Huang and X. Duan, *Nat. Nanotechnol.*, 2013, **8**, 952–958.

37 H. Zhang, *ACS Nano*, 2015.

38 J. N. Coleman, M. Lotya, A. O'Neill, S. D. Bergin, P. J. King, U. Khan, K. Young, A. Gaucher, S. De, R. J. Smith, I. V. Shvets, S. K. Arora, G. Stanton, H.-Y. H.-Y. Kim, K. Lee, G. T. Kim, G. S. Duesberg, T. Hallam, J. J. Boland, J. J. Wang, J. F. Donegan, J. C. Grunlan, G. Moriarty, A. Shmeliov, R. J. Nicholls, J. M. Perkins, E. M. Grieveson, K. Theuwissen, D. W. McComb, P. D. Nellist and V. Nicolosi, *Science*, 2011, **331**, 568–571.

39 P. Nguyen, J. Li, T. S. Sreeprasad, K. Jasuja, N. Mohanty, M. Ikenberry, K. Hohn, V. B. Shenoy and V. Berry, *Small*, 2013, **9**, 3823–3828.

40 Y. Zhang, L. Zhang and C. Zhou, *Acc. Chem. Res.*, 2013, **46**, 2329–2339.

41 H. Zhang, X. Lv, Y. Li, Y. Wang and J. Li, *ACS Nano*, 2010, **4**, 380–386.

42 B. Cho, J. Yoon, S. K. Lim, A. R. Kim, D.-H. Kim, S.-G. Park, J.-D. Kwon, Y.-J. Lee, K.-H. Lee, B. H. Lee, H. C. Ko and M. G. Hahm, *ACS Appl. Mater. Interfaces*, 2015, **7**, 16775–16780.

43 S. Behura, P. Nguyen, S. Che, R. Debbarma and V. Berry, *J. Am. Chem. Soc.*, 2015, **137**,

13060–13065.

44 D. a Dikin, S. Stankovich, E. J. Zimney, R. D. Piner, G. H. B. Dommett, G. Evmenenko, S. T. Nguyen and R. S. Ruoff, *Nature*, 2007, **448**, 457–460.

45 H. a. Becerril, J. Mao, Z. Liu, R. M. Stoltenberg, Z. Bao and Y. Chen, *ACS Nano*, 2008, **2**, 463–470.

46 K. Jasuja and V. Berry, *ACS Nano*, 2009, **3**, 2358–2366.

47 K. Jasuja, J. Linn, S. Melton and V. Berry, *J. Phys. Chem. Lett.*, 2010, **1**, 1853–1860.

48 S. Stankovich, D. a Dikin, G. H. B. Dommett, K. M. Kohlhaas, E. J. Zimney, E. a Stach, R. D. Piner, S. T. Nguyen and R. S. Ruoff, *Nature*, 2006, **442**, 282–286.

49 S. Park, N. Mohanty, J. W. Suk, A. Nagaraja, J. An, R. D. Piner, W. Cai, D. R. Dreyer, V. Berry and R. S. Ruoff, *Adv. Mater.*, 2010, **22**, 1736–1740.

50 Y. J. Mai, X. L. Wang, J. Y. Xiang, Y. Q. Qiao, D. Zhang, C. D. Gu and J. P. Tu, *Electrochim. Acta*, 2011, **56**, 2306–2311.

51 S.-L. Chou, J.-Z. Wang, M. Choucair, H.-K. Liu, J. A. Stride and S.-X. Dou, *Electrochem. commun.*, 2010, **12**, 303–306.

52 Q. Bao, H. Zhang, J. X. Yang, S. Wang, D. Y. Tang, R. Jose, S. Ramakrishna, C. T. Lim and K. P. Loh, *Adv. Funct. Mater.*, 2010, **20**, 782–791.

53 S. Watcharotone, D. a Dikin, S. Stankovich, R. Piner, I. Jung, G. H. B. Dommett, G. Evmenenko, S. E. Wu, S. F. Chen, C. P. Liu and S. T. Nguyen, *Nano Lett.*, 2007, **7**, 1888–1892.

54 T. Ouyang, Y. Chen, Y. Xie, K. Yang, Z. Bao and J. Zhong, *Nanotechnology*, 2010, **21**, 245701.

55 C. Y. Zhi, Y. Bando, C. C. Tang, H. Kuwahara and D. Golberg, *Adv. Mater.*, 2009, **21**, 2889–2890.

56 J. Wu and D. McLachlan, *Phys. Rev. B*, 1997, **56**, 1236–1248.

57 J. Wu and D. S. McLachlan, *Phys. Rev. B*, 1998, **58**, 14880–14887.

58 M. Paur, A. J. Molina-Mendoza, R. Bratschitsch, K. Watanabe, T. Taniguchi and T. Mueller, *Nat. Commun.*, 2019, **10**, 1709.

59 D. Joung, L. Zhai and S. I. Khondaker, *Phys. Rev. B*, 2011, **83**, 115323.

60 A. Mathkar, D. Tozier, P. Cox, P. Ong, C. Galande, K. Balakrishnan, A. Leela Mohana Reddy and P. M. Ajayan, *J. Phys. Chem. Lett.*, 2012, **3**, 986–991.

61 a. Hunt, E. Z. Kurmaev and a. Moewes, *Carbon N. Y.*, 2014, **75**, 366–371.

62 Y. Shen, S. Yang, P. Zhou, Q. Sun, P. Wang, L. Wan, J. Li, L. Chen, X. Wang, S. Ding and D. W. Zhang, *Carbon N. Y.*, 2013, **62**, 157–164.

63 W. S. Hummers and R. E. Offeman, *J. Am. Chem. Soc.*, 1958, **80**, 1339–1339.

64 D. R. Dreyer, S. Park, C. W. Bielawski and R. S. Ruoff, *Chem. Soc. Rev.*, 2010, **39**, 228–240.

65 Y. Zhou, Q. Bao, L. A. L. Tang, Y. Zhong and K. P. Loh, *Chem. Mater.*, 2009, **21**, 2950–2956.

66 S. Park, K.-S. Lee, G. Bozoklu, W. Cai, S. T. Nguyen and R. S. Ruoff, *ACS Nano*, 2008, **2**, 572–578.

67 S. Park, J. An, J. R. Potts, A. Velamakanni, S. Murali and R. S. Ruoff, *Carbon N. Y.*, 2011, **49**, 3019–3023.

68 C. Mattevi, G. Eda, S. Agnoli, S. Miller, K. A. Mkhoyan, O. Celik, D. Mastrogiovanni, G. Granozzi, E. Carfunkel and M. Chhowalla, *Adv. Funct. Mater.*, 2009, **19**, 2577–2583.

69 Y. Lin, T. V. Williams and J. W. Connell, *J. Phys. Chem. Lett.*, 2010, **1**, 277–283.

70 Y. M. Shi, C. Hamsen, X. T. Jia, K. K. Kim, A. Reina, M. Hofmann, A. L. Hsu, K. Zhang, H. N. Li, Z. Y. Juang, M. S. Dresselhaus, L. J. Li and J. Kong, *Nano Lett.*, 2010, **10**, 4134–4139.

71 D. Liu, W. Lei, S. Qin and Y. Chen, *Sci. Rep.*, 2014, **4**, 4453.

72 Y. Lin, T. V. Williams, T. B. Xu, W. Cao, H. E. Elsayed-Ali and J. W. Connell, *J. Phys. Chem. C*, 2011, **115**, 2679–2685.

73 I. Childres, L. Jauregui, W. Park, H. Cao and Y. Chen, in *New Developments in Photon and Materials Research*, 2013, pp. 1–20.

74 R. V. Gorbachev, I. Riaz, R. R. Nair, R. Jalil, L. Britnell, B. D. Belle, E. W. Hill, K. S. Novoselov, K. Watanabe, T. Taniguchi, A. K. Geim and P. Blake, *Small*, 2011, **7**, 465–468.

75 J. Tauc, R. Grigorovici and A. Vancu, *Phys. Status Solidi B*, 1966, **15**, 627–637.

76 S. K. Behura, S. Nayak, I. Mukhopadhyay and O. Jani, *Carbon N. Y.*, 2014, **67**, 766–774.

77 A. P. Nayak, A. Dolocan, J. Lee, H.-Y. Chang, T. Pandhi, M. Holt, L. Tao and D. Akinwande, *Nano*, 2013, **9**, 1450002.

78 U. Chandni, K. Watanabe, T. Taniguchi and J. P. Eisenstein, *Nano Lett.*, 2015, **15**, 7329–7333.

79 A. Popova, E. Sokolova, S. Raicheva and M. Christov, *Corros. Sci.*, 2003, **45**, 33–58.

80 X. Wu, M. Sprinkle, X. Li, F. Ming, C. Berger and W. A. De Heer, *Phys. Rev. Lett.*, 2008, **101**.

81 M. Städele, B. R. Tuttle and K. Hess, *J. Appl. Phys.*, 2001, **89**, 348–363.

82 J. G. Simmons, *J. Phys. D. Appl. Phys.*, 2002, 4, 613–657.

83 F.-C. Chiu, *Adv. Mater. Sci. Eng.*, 2014, **2014**, 18.

84 J. Frenkel, *Phys. Rev.*, 1938, **54**, 647–648.

85 T. S. Sreeprasad, A. A. Rodriguez, J. Colston, A. Graham, E. Shishkin, V. Pallem and V. Berry, *Nano Lett.*, 2013, **13**, 1757–1763.

86 S. S. Bamji, A. T. Bulinski and R. J. Densley, *IEEE Trans. Electr. Insul.*, 1989, **24**, 91–98.

87 C. H. Haake, *J. Appl. Phys.*, 1957, **28**, 245–250.

88 S. S. Bamji, A. T. Bulinski and R. J. Densley, *J. Appl. Phys.*, 1987, **61**, 694–699.

89 X. Wang and F. Xia, *Nat. Mater.*, 2015, **14**, 264–265.

90 M. Massicotte, P. Schmidt, F. Vialla, K. G. Schädler, a Reserbat-Plantey, K. Watanabe,

T. Taniguchi, K. J. Tielrooij and F. H. L. Koppens, *Nat. Nanotechnol.*, 2015, **11**, 1–6.

91 R. Debbarma, S. Behura, P. Nguyen, T. S. Sreeprasad and V. Berry, *ACS Appl. Mater. Interfaces*, 2016, **8**, 8721–8727.

92 Z. Wang, D.-K. Ki, H. Chen, H. Berger, A. H. MacDonald and A. F. Morpurgo, *Nat. Commun.*, 2015, **6**, 8339.

93 T. Yamaguchi, R. Moriya, Y. Inoue, S. Morikawa, S. Masubuchi, K. Watanabe, T. Taniguchi and T. Machida, *Appl. Phys. Lett.*, 2014, **105**, 223109.

94 B. Radisavljevic, A. Radenovic, J. Brivio, V. Giacometti and A. Kis, *Nat. Nanotechnol.*, 2011, **6**, 147–50.

95 K. Roy, M. Padmanabhan, S. Goswami, T. P. Sai, G. Ramalingam, S. Raghavan and A. Ghosh, *Nat. Nanotechnol.*, 2013, **8**, 826–830.

96 H. Tian, Z. Tan, C. Wu, X. Wang, M. A. Mohammad, D. Xie, Y. Yang, J. Wang, L.-J. Li, J. Xu and T.-L. Ren, *Sci. Rep.*, 2014, **4**, 5951.

97 S. Larentis, J. R. Tolsma, B. Fallahazad, D. C. Dillen, K. Kim, A. H. MacDonald and E. Tutuc, *Nano Lett.*, 2014, **14**, 2039–2045.

98 Y. Shi, W. Zhou, A.-Y. Lu, W. Fang, Y.-H. Lee, A. L. Hsu, S. M. Kim, K. K. Kim, H. Y. Yang, L.-J. Li, J.-C. Idrobo and J. Kong, *Nano Lett.*, 2012, **12**, 2784–2791.

99 H. Ago, H. Endo, P. Solís-Fernández, R. Takizawa, Y. Ohta, Y. Fujita, K. Yamamoto and M. Tsuji, *ACS Appl. Mater. Interfaces*, 2015, **7**, 5265–5273.

100 D. Xiao, G. Bin Liu, W. Feng, X. Xu and W. Yao, *Phys. Rev. Lett.*, 2012, **108**.

101 A. M. Jones, H. Yu, N. J. Ghimire, S. Wu, G. Aivazian, J. S. Ross, B. Zhao, J. Yan, D. G. Mandrus, D. Xiao, W. Yao and X. Xu, *Nat. Nanotechnol.*, 2013, **8**, 634–8.

102 L. Hu, X. Hu, X. Wu, C. Du, Y. Dai and J. Deng, *Phys. B Condens. Matter*, 2010, **405**, 3337–3341.

103 C. Cao, M. Wu, J. Jiang and H. P. Cheng, *Phys. Rev. B - Condens. Matter Mater. Phys.*, 2010, **81**.

104 K. T. Chan, J. B. Neaton and M. L. Cohen, *Phys. Rev. B - Condens. Matter Mater. Phys.*, 2008, **77**.

105 S. Y. Chen, C. Zheng, M. S. Fuhrer and J. Yan, *Nano Lett.*, 2015, **15**, 2526–2532.

106 Y. Wang, Z. Xia, L. Liu, W. Xu, Z. Yuan, Y. Zhang, H. Sirringhaus, Y. Lifshitz, S.-T. Lee, Q. Bao and B. Sun, *Adv. Mater.*, 2017, **29**, 1606370.

107 X. Li, W. Cai, J. An, S. Kim, J. Nah, D. Yang, R. Piner, A. Velamakanni, I. Jung, E. Tutuc, S. K. Banerjee, L. Colombo and R. S. Ruoff, *Science (80-.).*, 2009, **324**, 1312–1314.

108 A. Reina, X. Jia, J. Ho, D. Nezich, H. Son, V. Bulovic, M. S. Dresselhaus and K. Jing, *Nano Lett.*, 2009, **9**, 30–35.

109 S. Bae, H. Kim, Y. Lee, X. Xu, J.-S. Park, Y. Zheng, J. Balakrishnan, T. Lei, H. Ri Kim, Y. Il Song, Y.-J. Kim, K. S. Kim, B. Özyilmaz, J.-H. Ahn, B. H. Hong and S. Iijima, *Nat. Nanotechnol.*, 2010, **5**, 574–578.

110 C. C. Chen, M. Aykol, C. C. Chang, A. F. J. Levi and S. B. Cronin, *Nano Lett.*, 2011, **11**, 1863–1867.

111 Y. Song, X. Li, C. Mackin, X. Zhang, W. Fang, T. Palacios, H. Zhu and J. Kong, *Nano Lett.*, 2015, **15**, 2104–2110.

112 D. Sinha and J. U. Lee, *Nano Lett.*, 2014, **14**, 4660–4664.

113 X. Miao, S. Tongay, M. K. Petterson, K. Berke, A. G. Rinzler, B. R. Appleton and A. F. Hebard, *Nano Lett.*, 2012, **12**, 2745–2750.

114 E. Shi, H. Li, L. Yang, L. Zhang, Z. Li, P. Li, Y. Shang, S. Wu, X. Li, J. Wei, K. Wang, H. Zhu, D. Wu, Y. Fang and A. Cao, *Nano Lett.*, 2013, **13**, 1776–1781.

115 V. G. Kravets, A. N. Grigorenko, R. R. Nair, P. Blake, S. Anissimova, K. S. Novoselov and A. K. Geim, *Phys. Rev. B*, 2010, **81**, 155413.

116 M. Bernardi, M. Palummo and J. C. Grossman, *Nano Lett.*, 2013, **13**, 3664–3670.

117 S.-E. E. Zhu, S. Yuan and G. C. A. M. A. M. Janssen, *EPL (Europhysics Lett.*, 2014, **108**,

17007.

118 M. Chhowalla, H. S. Shin, G. Eda, L.-J. Li, K. P. Loh and H. Zhang, *Nat. Chem.*, 2013, **5**, 263–275.

119 A. Kuc, N. Zibouche and T. Heine, *Phys. Rev. B*, 2011, **83**, 245213.

120 C. Lan, C. Li, Y. Yin and Y. Liu, *Nanoscale*, 2015, **7**, 5974–5980.

121 K. M. McCreary, A. T. Hanbicki, G. G. Jernigan, J. C. Culbertson and B. T. Jonker, *Sci. Rep.*, 2016, **6**, 19159.

122 H. Tan, Y. Fan, Y. Rong, B. Porter, C. S. Lau, Y. Zhou, Z. He, S. Wang, H. Bhaskaran and J. H. Warner, *ACS Appl. Mater. Interfaces*, 2016, **8**, 1644–1652.

123 S. Behura, K. C. Chang, Y. Wen, R. Debbarma, P. Nguyen, S. Che, S. Deng, M. R. Seacrist and V. Berry, *IEEE Nanotechnol. Mag.*, 2017, 11, 33–38.

124 A. Berkdemir, H. R. Gutiérrez, A. R. Botello-Méndez, N. Perea-López, A. L. Elías, C.-I. Chia, B. Wang, V. H. Crespi, F. López-Urías, J.-C. Charlier, H. Terrones and M. Terrones, *Sci. Rep.*, 2013, **3**, 1755.

125 L. M. Malard, M. A. Pimenta, G. Dresselhaus and M. S. Dresselhaus, *Phys. Rep.*, 2009, **473**, 51–87.

126 H. Zeng, G.-B. Liu, J. Dai, Y. Yan, B. Zhu, R. He, L. Xie, S. Xu, X. Chen, W. Yao and X. Cui, *Sci. Rep.*, 2013, **3**, 1608.

127 A. Ferrari and D. Basko, *Nat. Nanotechnol.*, 2013, **8**, 235–46.

128 Q. Wang, T. Soderstrom, K. Omaki, A. Lennon and S. Varlamov, in *Energy Procedia*, 2012, vol. 15, pp. 220–228.

129 X. X. Li, H. Zhu, K. Wang, A. Cao, J. Wei, C. Li, Y. Jia, Z. Li, X. X. Li and D. Wu, *Adv. Mater.*, 2010, **22**, 2743–2748.

130 J. M. Shah, Y. Li, T. Gessmann and E. Fred Schubert, *MRS Proc.*, 2003, **798**, Y7.11.

131 A. Kumar and P. K. Ahluwalia, *Phys. B Condens. Matter*, 2012, **407**, 4627–4634.

132 K. Chen, X. Wan, W. Xie, J. Wen, Z. Kang, X. Zeng, H. Chen and J. Xu, *Adv. Mater.*, 2015, **27**, 6431–6437.

133 X. Wan, Y. Xu, H. Guo, K. Shehzad, A. Ali, Y. Liu, J. Yang, D. Dai, C.-T. Lin, L. Liu, H.-C. Cheng, F. Wang, X. Wang, H. Lu, W. Hu, X. Pi, Y. Dan, J. Luo, T. Hasan, X. Duan, X. Li, J. Xu, D. Yang, T. Ren and B. Yu, *npj 2D Mater. Appl.*, 2017, **1**, 4.

134 H. Qiu, T. Xu, Z. Wang, W. Ren, H. Nan, Z. Ni, Q. Chen, S. Yuan, F. Miao, F. Song, G. Long, Y. Shi, L. Sun, J. Wang and X. Wang, *Nat. Commun.*, 2013, **4**, 2642.

135 S. Tongay, J. Suh, C. Ataca, W. Fan, A. Luce, J. S. Kang, J. Liu, C. Ko, R. Raghunathanan, J. Zhou, F. Ogletree, J. Li, J. C. Grossman and J. Wu, *Sci. Rep.*, 2013, **3**, 2657.

136 N. Peimyoo, W. Yang, J. Shang, X. Shen, Y. Wang and T. Yu, *ACS Nano*, 2014, **8**, 11320–11329.

137 T. Kato and T. Kaneko, *ACS Nano*, 2016, **10**, 9687–9694.

138 N. Peimyoo, J. Shang, C. Cong, X. Shen, X. Wu, E. K. L. Yeow and T. Yu, *ACS Nano*, 2013, **7**, 10985–10994.

139 A. Chernikov, T. C. Berkelbach, H. M. Hill, A. Rigosi, Y. Li, O. B. Aslan, D. R. Reichman, M. S. Hybertsen and T. F. Heinz, *Phys. Rev. Lett.*, 2014, **113**, 076802.

140 B. Zhu, X. Chen and X. Cui, *Sci. Rep.*, 2015, **5**, 9218.

141 A. A. Mitioglu, P. Plochocka, J. N. Jadczak, W. Escoffier, G. L. J. A. Rikken, L. Kulyuk and D. K. Maude, *Phys. Rev. B*, 2013, **88**, 245403.

142 K. F. Mak, K. He, C. Lee, G. H. Lee, J. Hone, T. F. Heinz and J. Shan, *Nat. Mater.*, 2012, **12**, 207–211.

143 U. Dutta and P. Chatterjee, *J. Appl. Phys.*, 2004, **96**, 2261–2271.

144 T. K. Todorov, T. Gershon, O. Gunawan, C. Sturdevant and S. Guha, *Appl. Phys. Lett.*, 2014, **105**, 173902.

145 A. Hadipour, B. De Boer and P. W. M. Blom, *Adv. Funct. Mater.*, 2008, **18**, 169–181.

146 I. Mathews, D. O'Mahony, B. Corbett and A. P. Morrison, *Opt. Express*, 2012, **20**, A754.

147 Y. Zou, Z. Deng, W. J. Potscavage, M. Hirade, Y. Zheng and C. Adachi, *Appl. Phys. Lett.*, 2012, **100**, 243302.

148 L. Y. Gan, Q. Zhang, Y. Cheng and U. Schwingenschlögl, *J. Phys. Chem. Lett.*, 2014, **5**, 1445–1449.

149 H. Li, Q. Zhang, C. C. R. Yap, B. K. Tay, T. H. T. Edwin, A. Olivier and D. Baillargeat, *Adv. Funct. Mater.*, 2012, **22**, 1385–1390.

150 J. Tamayo, R. García and R. Garcia, *Langmuir*, 1996, **12**, 4430–4435.

151 J. Tamayo and R. García, *Appl. Phys. Lett.*, 1998, **73**, 2926.

152 N. F. Martínez and R. García, *Nanotechnology*, 2006, **17**, S167.

153 S. Ghatak, A. N. Pal and A. Ghosh, *ACS Nano*, 2011, **5**, 7707–7712.

154 D. Jariwala, V. K. Sangwan, D. J. Late, J. E. Johns, V. P. Dravid, T. J. Marks, L. J. Lauhon and M. C. Hersam, *Appl. Phys. Lett.*, 2013, **102**, 173107.

155 G. He, K. Ghosh, U. Singisetti, H. Ramamoorthy, R. Somphonsane, G. Bohra, M. Matsunaga, A. Higuchi, N. Aoki, S. Najmaei, Y. Gong, X. Zhang, R. Vajtai, P. M. Ajayan and J. P. Bird, *Nano Lett.*, 2015, **15**, 5052–5058.

156 B. Ricco and M. Y. Azbel, *Phys. Rev. B*, 1984, **29**, 1970–1981.

157 Jian Ping Sun, G. I. Haddad, P. Mazumder and J. N. Schulman, *Proc. IEEE*, 1998, **86**, 641–660.

158 H. M. Hill, A. F. Rigosi, K. T. Rim, G. W. Flynn and T. F. Heinz, *Nano Lett.*, 2016, **16**, 4831–4837.

159 Z. Gong, G.-B. Liu, H. Yu, D. Xiao, X. Cui, X. Xu and W. Yao, *Nat. Commun.*, 2013, **4**, 2053.

VITA

EDUCATION

- **University of Illinois at Chicago** Aug 2014- May 2020
  PhD Candidate, Chemical Engineering
- **Indian Institute of Technology Bombay** July 2010- June 2014
  Bachelor of Technology, Chemical Engineering

TEACHING

Teaching Assistant Aug 2014-December 2019

Chemical Engineering Department, UIC

- CHE 301/CHE 321: Led weekly discussion sessions and tutorials and graded homework, exams and projects for chemical engineering thermodynamics (301) and chemical reaction engineering (321)
- CHE 381/CHE 382: Led weekly laboratory sessions on heat, momentum and mass transfer operations associated with chemical processes for 30-35 senior undergraduate students

PUBLICATIONS

- Aaditya Pendse, Semih Cetindag, Meng-Hsuan Lin, Angelina Rackovic, **Rousan Debbarma**, Soroush Almassi, Brian P. Chaplin, Vikas Berry, Jerry W. Shan, and Sangil Kim, "Charged Layered Boron Nitride-Nanoflake Membranes for Efficient Ion Separation and Water Purification", *Small* 2019, 1904590
- Shikai Deng, Songwei Che, **Rousan Debbarma**, and Vikas Berry, "Strain in Single-Wrinkle on MoS_2-Flake for in-plane Realignment of Band-Structure for Enhanced Photo-Response", *Nanoscale***,** 11, 504-511, 2019
- **Rousan Debbarma**, Sanjay Behura, Yu Wen, Songwei Che, and Vikas Berry, "WS_2-Induced Enhanced Optical Absorption and Efficiency in Graphene/Silicon Heterojunction Photovoltaic Cells", *Nanoscale*, 10, 20218-20225, 2018

- Sanjay Behura, Phong Nguyen, **Rousan Debbarma**, Songwei Che, Michael Seacrist and Vikas Berry, "Chemical Interaction Guided, Metal-Free Growth of Large-Area Hexagonal Boron Nitride on Silicon-Based Substrates", *ACS Nano*, 11 (5), 4985-4994, 2017
- Sanjay Behura, Kai-Chih Chang, Yu Wen, **Rousan Debbarma**, Phong Nguyen, Songwei Che, Shikai Deng, Michael Seacrist, and Vikas Berry, "WS_2/Silicon Heterojunction Solar Cells", *IEEE Nanotechnology Magazine*, 11 (2), 33-38, 2017
- Vedhikha T. Parthasarathy, **Rousan Debbarma**, Sanjay Behura, Phong Nguyen, Yu Wen, Dylan Lynch, and Vikas Berry, "Facile Solution Processed MoS_2-PEDOT:PSS Mixed Structure as Flexible Paper-Based Infra-Red Sensor", *Science Advances Today*, 3, 25268, 2017
- **Rousan Debbarma**, Sanjay Behura, Phong Nguyen, T. S. Sreeprasad, and Vikas Berry, "Electrical Transport and Network Percolation in Graphene and Boron Nitride Mixed-Platelet Structures", *ACS Applied Materials and Interfaces*, 8 (13), 8721-8727, 2016
- **Rousan Debbarma** and Ateeque Malani, "Comparative Study of Water Adsorption on H^+ and K^+ ion Exposed Mica Surface: Monte Carlo Simulation Study", *Langmuir*, 32 (4), 1034–1046, 2016
- Sanjay Behura, Phong Nguyen, Songwei Che, **Rousan Debbarma**, and Vikas Berry, "Large-Area, Transfer-Free, Oxide-Assisted, Synthesis of Hexagonal Boron Nitride Films and their Heterostructures with MoS_2 and WS_2", *Journal of American Chemical Society*, 137 (40), 13060-65, 2015

Journal Copyright Statement

Electrical Transport and Network Percolation in Graphene and Boron Nitride Mixed-Platelet Structures

Author:
Rousan Debbarma, Sanjay Behura, Phong Nguyen, et al
Publication:
Applied Materials
Publisher:
American Chemical Society
Date:
Apr 1, 2016

WS_2-induced enhanced optical absorption and efficiency in graphene/silicon heterojunction photovoltaic cells

R. Debbarma, S. K. Behura, Y. Wen, S. Che and V. Berry, *Nanoscale*, 2018, 10, 20218
DOI: 10.1039/C8NR03194K